Engineering Geology 346 (2025) 107902

Contents lists available at ScienceDirect

Engineering Geology

journal homepage: www.elsevier.com/locate/enggeo

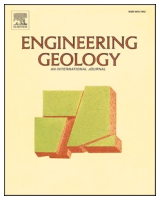

Integrated geological modeling of partially exposed Precambrian bedrock surface and thickness of overlying Quaternary deposits

Teemu Lindqvist [a,b,*], Eemi Ruuska [a], Emilia Kosonen [b], Noora Hornborg [b], Pietari Skyttä [a,e], Niko Putkinen [c], Juho Mansikkamäki [d]

[a] Department of Geography and Geology, FI-20014 University of Turku, Finland
[b] Geological Survey of Finland, P.O. Box 96, FI-02151 Espoo, Finland
[c] Geological Survey of Finland, P.O. Box 97, FI-67101 Kokkola, Finland
[d] AFRY Finland Oy, P.O. Box 4, FI-33900 Tampere, Finland
[e] Structural Geology Company Oy, Kaniikintie 3, FI-20300 Turku, Finland

ARTICLE INFO

Keywords:
3D geological model
Bedrock surface topography
Crystalline bedrock
Structural geology
Deformation zone
Superficial deposit

ABSTRACT

Bedrock surface topography and thickness of the overlying sediments are key information for numerous engineering applications. However, discrete geological structures, such as bedrock deformation zones, which cause abrupt breaks along bedrock surface, remain largely unrecognized within the conventional digital elevation models (DEMs). This paper provides an example over the generation of geological 3D-models which integrate the deformation zone-controlled erosion surface of the Precambrian crystalline bedrock and the associated thickness variation of the overlying Quaternary glacial sediments in southern Fennoscandian shield. We interpreted the deformation zones from 2D geological and geophysical maps as well as topographic signatures along conventional bedrock surface-DEM, which is based on bedrock surface elevation points comprising >87,000 geotechnical ground investigations, Light Detection and Ranging (LiDAR) and acoustic-seismic datasets. We classified the resulting final deformation zone traces into major, intermediate, and minor classes based on their cross-cutting relationships and lengths, and further used this information in generating an improved, structurally constrained bedrock surface-DEM. As input for the improved bedrock surface-DEM, we assigned the recognized 19 m, 11 m, and 5 m thickness of the load bearing stratum (LBS; basal till, gravel, coarse sand) for the major, intermediate, and minor deformation zones, respectively, and modified the bedrock surface accordingly. The resulting structurally constrained bedrock surface-DEM highlights the pronounced erosion and continuity of the linear topographic depressions occurring along the bedrock surface. The resulting network of linear depressions honors the topology and continuity of the bedrock deformation zones and provides geologically justified depth-to-bedrock constraints also in those areas where very limited geotechnical data is available, and, consequently, the conventional approaches result in excessively high bedrock surface elevations and overly thin overburden. By contrast, areas outside the deformation zones show up to 3 m thick LBS, which indicates that there is no need for bedrock-DEM improvements in those areas. The results can be used for e.g. detailed analysis of seismic hazard associated with the soil amplification, and development of improved bedrock surface modeling methods.

1. Introduction

Requirements for improving the representativity of geological subsurface models are increasing due to challenging application areas, and failures resulting from inaccurate geological models are likely to cause delayed schedules, reduced productivity, and underestimated costs. Many of the challenges within such cases arise from inadequate spatial coverage, quality, or resolution of the primary data, followed by processing and interpretations that require profound understanding of the geological conditions and evolution of the modeling target (Thierry et al., 2009; Cassidy et al., 2014; Bond et al., 2015; Ojala et al., 2021; Madsen et al., 2022; Giacomelli et al., 2023). Consequently, the generated models often remain generalizations that fail in representing the present-day structure and composition of the subsurface (Bowden, 2004;

* Corresponding author at: Geological Survey of Finland, P.O. Box 96, FI-02151 Espoo, Finland.
E-mail addresses: teemu.lindqvist@gtk.fi (T. Lindqvist), eeolru@utu.fi (E. Ruuska), emilia.kosonen@gtk.fi (E. Kosonen), noora.hornborg@gtk.fi (N. Hornborg), pietari@sgeo.fi (P. Skyttä), niko.putkinen@gtk.fi (N. Putkinen), juho.mansikkamaki@afry.com (J. Mansikkamäki).

https://doi.org/10.1016/j.enggeo.2024.107902
Received 12 June 2024; Received in revised form 12 December 2024; Accepted 31 December 2024
Available online 3 January 2025

Lee, 2016; Høyer et al., 2019; Baynes et al., 2021; Kim et al., 2020; Yan et al., 2023). Among the most significant geological components in e.g. groundwater studies, geotechnical engineering, and mineral exploration are the topography of bedrock surface and the thickness of overburden as their properties set the boundary conditions for these applications (e.g. Paulen et al., 2006; Chung and Rogers, 2012; Cassidy et al., 2014; Olayanju et al., 2017; Setiawan et al., 2018; Abbaszadeh Shahri et al., 2021; Spadi et al., 2022).

Compilation of the digital elevation models over the bedrock surface topography (hereafter bedrock-DEM) typically utilizes sparse and variably reliable bedrock surface elevation points from multiple source datasets, and their subsequent interpolation into 3D-surfaces (Paulen et al., 2006; Chung and Rogers, 2012; Van Hoesen, 2014; Chesnaux et al., 2011, 2017; Popovs et al., 2022). Significant emphasis has been given to distinguishing the "verified" bedrock surface elevation points derived from e.g. percussion drilling from those that have less reliable elevation constraints. This is typically followed by geostatistical analysis of the quantity, density, and spatial distribution of the data points, and subsequent selection of the most suited interpolation method for the respective dataset and the modeling purpose (Paulen et al., 2006; Erdogan, 2009; Chung and Rogers, 2012; Van Hoesen, 2014; Chesnaux et al., 2017). The accuracy and precision of the interpolation results are commonly evaluated to the difference of elevation values between the models and a validation dataset by using e.g. the Root Mean Square Error (RMSE; e.g. Zimmerman et al., 1999; Erdogan, 2009; Abbaszadeh Shahri et al., 2021) method.

Major challenges associated with surface interpolation relate to the surface irregularity, and the sparse and clustered character of the input data (Zimmerman et al., 1999; Gong et al., 2000; Skyttä et al., 2015; Chesnaux et al., 2017; Salekin et al., 2018; Chetty and Tesfamichael, 2021; Popovs et al., 2022; Ruuska et al., 2023). Surface irregularity of bedrock-DEMs can be addressed by including a factor of anisotropy into the surface interpolation, which allows emphasizing uniform topographic trends but fails when contrasting structural trends are present (e.g. Paulen et al., 2006; Ruuska et al., 2023). The sparseness of the input data has been addressed by e.g. interpreting additional data points between boreholes using (i) geological cross-sections (Chesnaux et al., 2017), (ii) geophysical datasets (Cassidy et al., 2014; Ruuska et al., 2023), or (iii) using artificial intelligence (AI) based methods (Abbaszadeh Shahri et al., 2020), which result in improved estimates in depth-to-the-bedrock but still do not adequately address the lateral continuity of the topographic lows along the bedrock-DEM.

In areas characterized by glacially eroded crystalline bedrock (e.g. Fennoscandian and Canadian Shields), much of the bedrock surface topography is controlled by the deformation zones (faults, shear zones) within the bedrock, and their selective glacial erosion (Krabbendam and Bradwell, 2014; Ruuska et al., 2023; Skyttä et al., 2023). The resulting features are elongate topographic depressions characterized by significant vertical breaks along the bedrock-DEM across short lateral distances (Skyttä et al., 2015, 2023; Ruuska et al., 2023) and thick overlying sediments (Saresma et al., 2021). In this context, the lack of the verified bedrock surface elevation data from the topographic depressions (with thick overburden) and the complexity of the linear topographic depressions (comprising multiple orientations, sizes, and cross-cutting relationships; e.g. Sanderson and Nixon, 2015) are major issues which no conventional solutions can address, and no validation methods (e.g. the RMSE) are useful to evaluate the quality of the results.

Regarding the recent advances in bedrock-DEM modeling, Chesnaux et al. (2017, 2011) provided improved geological context for the models through adding bedrock surface elevation points from geological cross-sections between boreholes. However, the elevation of the additional bedrock surface points is subject to the uncertainties associated with the geological interpretation, and the models did not systematically take into account the lateral continuity of the topographic lows. Skyttä et al. (2015) and Ruuska et al. (2023) modeled the abrupt vertical bedrock surface breaks by using break lines or 3D-surfaces along which the bedrock-DEM was edited "manually". However, these studies had limited understanding about the dimensions of the linear bedrock surface depressions, resulting in significantly generalized lengths, widths and depths of the linear depressions and underdeveloped structural networks. The AI-based methods have shown promise in automated prediction of depth to bedrock values in areas where no verified bedrock elevation data is available (Abbaszadeh Shahri et al., 2020, 2021; Lysdahl et al., 2022). However, as the training datasets comprise plain xyz-points and no further constraints of the discrete bedrock structures were included in the source data, the algorithm has very limited capability to predict the abrupt breaks and the associated linear topographic lows along the bedrock surface as those are typically the areas of the lowest density of input point data. Attempts towards including constraints about the lateral continuity of discrete geological features recognized from airborne geophysics have been tested through combining them with drilling data, followed by processing with AI-methods (Lysdahl et al., 2022). However, the earlier stated problems still remain as the geophysical data is prone to uncertainties in constraining realistic overburden thicknesses, and the geophysical data was not used to delineate the deformation zones, and their networks.

In this paper, we use a novel approach that integrates systematic analysis of the bedrock structures, with specific reference to the 2D-continuity and networking of bedrock deformation zones, with depth-to-bedrock data, and hence provides an improved framework for using geotechnical datasets to compile geologically justified bedrock surface DEMs. The approach results in an improved bedrock-DEM which both honors the input dataset but also reflects the geologically justified structural character of the bedrock surface. Our results further show that the thickness of the load-bearing stratum (basal till, gravel, coarse sand; hereafter LBS) within the fracture-controlled erosional topographic depressions associated with bedrock deformation zones may be at least six times thicker than within the surrounding areas characterized by less intense, distributed fracturing (Fig. 1). Overall, the new models significantly decrease the epistemic uncertainty (e.g. Baynes et al., 2021) of the subsurface models and provide a major improvement of modeling in complex geological settings. The results of this study have specific applicability to detailed analysis of the seismic hazard related to soil amplification (e.g. Baise et al., 2016; Lee et al., 2021), and development of advanced bedrock surface modeling methods.

The site of the investigation is located in southern Finland where the bedrock is characterized by complexly deformed 1.9–1.8 Ga Paleoproterozoic rocks (Pajunen et al., 2008). The glacially eroded bedrock surface is overlain by laterally extensive glacial basal tills and more limited occurrences of coarse grained glacifluvial sediments (gravel and sand) with 1–15 m thicknesses (Haavisto and Kukkonen, 1975; Haavisto-Hyvärinen et al., 1996). These are further overlain by fine-grained sediments (dominantly clay) that were deposited as basin-infills, presently reaching maximum thicknesses of 20–25 m (Ojala et al., 2021; Saresma et al., 2021). The principal dataset used in this study comprised elevation point data from >87,000 geotechnical ground investigations, LiDAR-surveys from exposed bedrock areas, and 90 km of acoustic-seismic data from marine areas. The 2D structural geological interpretations were generated using regional bedrock map, foliation data, aeromagnetic maps, and regional elevation models.

2. Geologic setting

2.1. Bedrock

The study area is located within the southern part of the Fennoscandian shield, which is characterized by high-grade metamorphic rocks that were formed as response to the complex and prolonged Svecofennian orogeny at 1.9–1.8 Ga (Lahtinen et al., 2005; Pajunen et al., 2008; Fig. 2). Towards the later stages of the orogeny (< 1.83 Ga), the previously penetrative regional deformation became more partitioned, which in southern Finland led to the generation of the dominantly E and

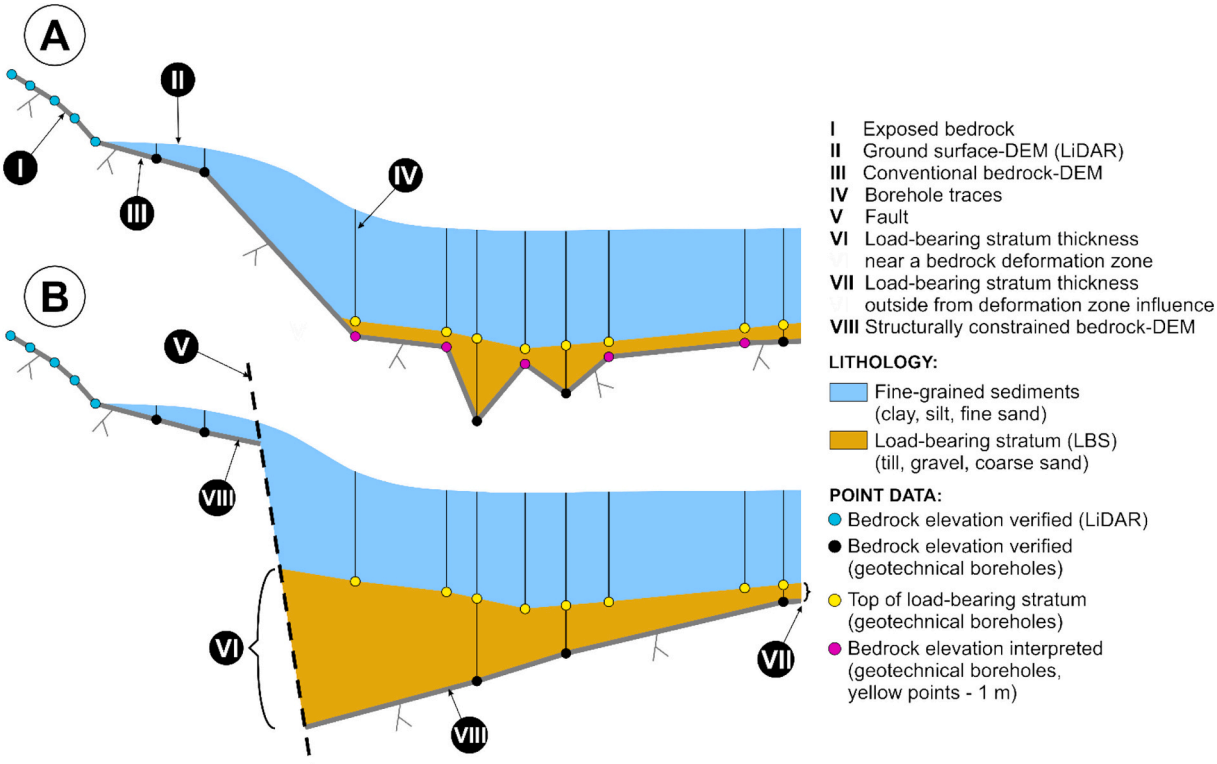

Fig. 1. Schematic illustrations of contrasting approaches in modeling the bedrock surface topography (grey lines in A and B) and its effect on the thickness of overlying sediments. A) Conventional bedrock surface-DEM generated from verified bedrock surface points and interpreted bedrock surface points that are based on fixed thickness estimate of the overlying LBS. B) An improved, structurally constrained bedrock-DEM that considers the verified bedrock surface points and the presence of a bedrock deformation zone resulting in a significant increase in the thickness of the LBS.

NE trending crustal-scale shear zones (Ehlers et al., 1993; Skyttä and Mänttäri, 2008; Torvela et al., 2008; Torvela and Kurhila, 2022; Fig. 2A). The most important shear zones are the E trending South Finland, Somero-Karkkila and Hyvinkää Shear Zones, which are dominantly strike-slip in character (Fig. 2; SFSZ, SKSZ and HSZ, respectively; Väisänen and Skyttä, 2007; Pajunen et al., 2008; Torvela et al., 2008; Torvela and Kurhila, 2022). The NE trending Kisko and Porkkala-Mäntsälä, and to lesser extent the N trending Vuosaari-Korso, and the NNW trending Jyly Shear Zones (Fig. 2; Kisko SZ, PMSZ, VKSZ, Jyly SZ, respectively) have either dip- or strike-slip character, typically abut against the larger E trending shear zones, and as such, contribute to the segmentation of the crust into shear-zone bound crustal blocks.

The transition of the regional deformation regime from ductile to brittle occurred at ca. 1.75 Ga (Mattila and Viola, 2014; Nordbäck et al., 2022). The most significant post-Svecofennian events within the surroundings of the study area comprise the emplacement of the anorogenic 1.65–1.54 Ga Bodom and Obbnäs rapakivi batholiths (Kosunen, 2004) and their subsequent brittle deformation (Elminen et al., 2008). Generation of new brittle structures and reactivation of the existing ones within the southern part of the Fennoscandian Shield continued at specific intervals until ca. 0.55 Ga, where the youngest events are related to the Caledonian orogeny (Mattila and Viola, 2014; Nordbäck et al., 2022).

The study area covers an area of approximately 80 km^2 and is located to the east of the PMSZ (Fig. 2), where the lithology comprises 1.90–1.86 Ga quartz feldspar gneisses and paragneisses (grouped as gneiss), 1.90–1.86 Ga mafic volcanic rocks and amphibolites (grouped as amphibolite), 1.89–1.87 Ga granodiorites, 1.89–1.87 Ga gabbros, 1.89–1.87 Ga peridotites, and 1.84–1.77 Ga granites (Korsman et al., 1997; Kähkönen, 2005; Pajunen et al., 2008). The ductile structures are dominated by km-scale open to isoclinal folds with E trending axial surfaces (Fig. 2B). The fold limbs are frequently disrupted by ductile shear zones or faults resulting in partly segmented limbs (Fig. 2B). Ductile shear zones include foliation-parallel E and ENE trending zones and NE trending zones, which distinctly truncate the Svecofennian ductile deformation patterns (Elminen et al., 2008). The foliation-parallel shear zones dip steeply or sub-vertically towards S or SSE and display mostly reverse, south side up sense of shear (Elminen et al., 2008; Fig. 2B). The NE trending zones dip steeply to sub-vertically towards SE and show SE side up reverse sense of shear with a sinistral strike-slip component.

Faults within the Helsinki-Espoo region display NE, WNW, NNW, N, and E trends (Elminen et al., 2008). The NE trending faults are dominated by reactivated NE trending ductile shear zones, such as the major PMSZ (Fig. 2A), which is characterized by at least one brittle reactivation with sub-horizontal dextral (cf. predating ductile deformation has sinistral component) movement sense. The PMSZ has been dated to 1300–950 Ma using the $^{40}Ar/^{39}Ar$ method (Heeremans and Wijbrans, 1999), and the age has been interpreted as the reactivation age (Elminen et al., 2008). The steep to sub-vertical WNW and NNW trending faults are the most abundant faults and they show an orthorhombic fault network pattern crosscutting the Svecofennian ductile deformation patterns and the Bodom and Obbnäs rapakivi batholiths in the area (Elminen et al., 2008). Their kinematics show both normal fault and strike-slip conditions. The N trending faults are strike-slip faults with successive sinistral and dextral movement phases, and they are younger than the WNW and NNW trending normal faults. The E trending faults were generated with or without ductile precursors and are associated with both sinistral and dextral apparent displacements of older fabrics. Furthermore, low-angle reverse faults with diverse dip directions have been observed in the Helsinki-Espoo region. Glacially induced faults (GIFs) have not been found from the study area as their occurrence is restricted to more northerly areas within the Fennoscandia (Sutinen et al., 2021).

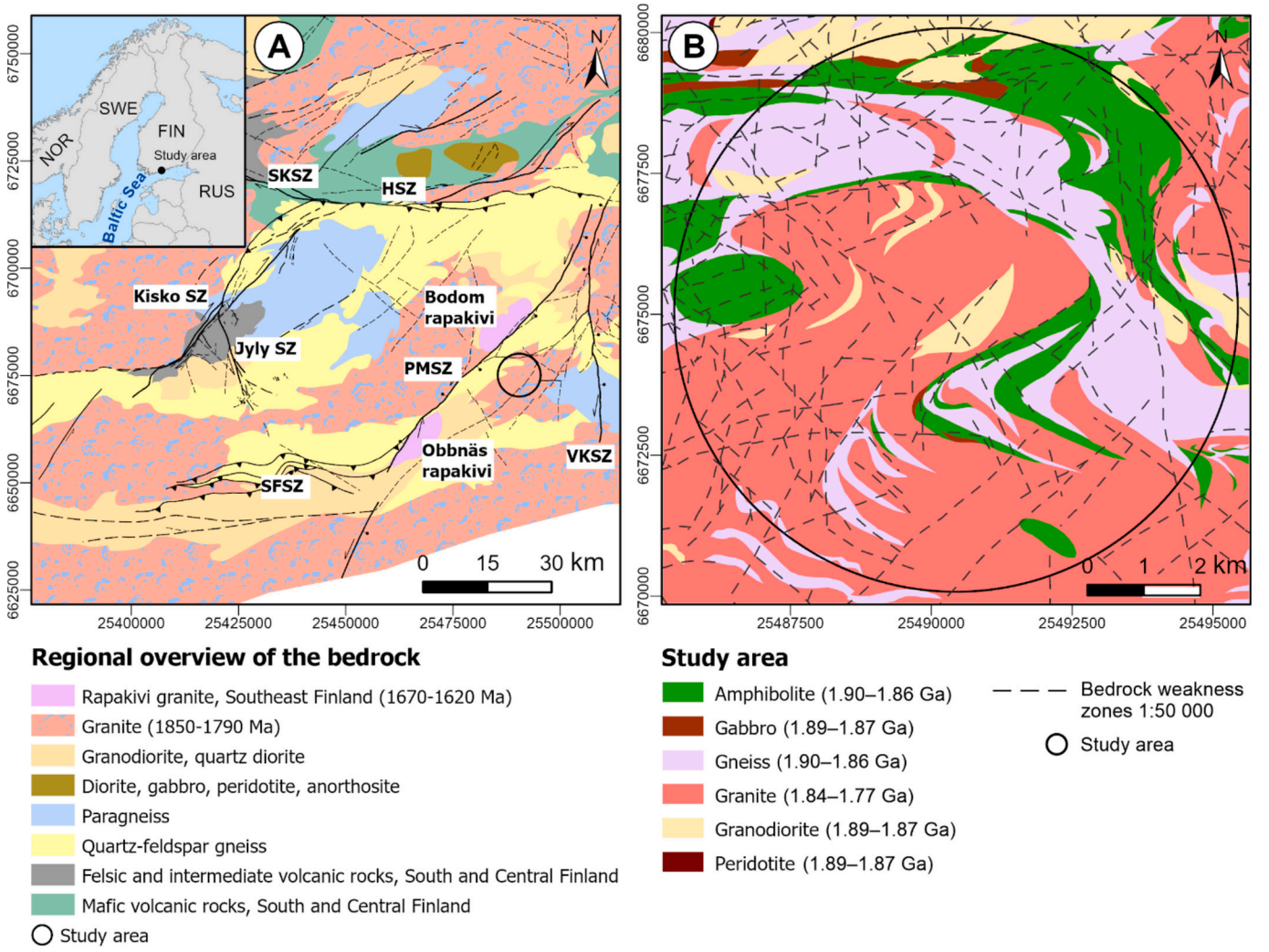

Fig. 2. A) Regional overview of the bedrock lithology and major shear zones (Bedrock of Finland 1:10000000, 2019; Bedrock of Finland scale free, 2022 © Geological Survey of Finland; hereafter GTK). SKSZ = Somero-Karkkila SZ, HSZ = Hyvinkää SZ, PMSZ = Porkkala-Mäntsälä SZ, SFSZ = South Finland SZ, VKSZ = Vuosaari-Korso SZ. B) Bedrock lithology (modified after Bedrock of Finland 1:200000, 2022 © GTK), and weakness zone traces (Bedrock weakness zones 1:50000, 2020 © GTK) within the study area.

The most prominent fracture sets within the Helsinki-Espoo region show sub-vertical or steeply dipping attitudes and NE and NW trends (Wennerström et al., 2008), of which the NE trending fractures are controlled by the regional foliation. Based on their orientation and systematic occurrence throughout the Helsinki-Espoo region, they are attributed to regional deformation. The other fracture sets trend E, NNE, N and WNW. Despite the regional character of the fractures, their intensity increases within vicinity of the faults (Wennerström et al., 2008; Fig. 2B).

2.2. *Superficial deposits*

The study area is located along the northern coast of Gulf of Finland, in the eastern Baltic Sea (Fig. 2A, 3), where the area has undergone ultra-slow cratonic denudation due to the burial – erosion cycles spanning hundreds of millions of years (Hall et al., 2021). The majority of superficial deposits and landforms in southern Finland are associated with cooling and warming episodes between 70 and 12 ka BP (Benn and Evans, 2010), and particularly the Late Weichselian stage (25–13 ka) when the retreat of the Fennoscandian Ice Sheet (FIS) caused glacial erosion due to onsetting ice streams as well as deposition of glacial and pre-existing sediments. The lowermost sediments overlying the crystalline bedrock within the study area are characterized by two distinct basal till units (Bouchard et al., 1990) with an inter-layer of sand and fine-grained sediments (Rainio and Lahermo, 1976; Hirvas and Nenonen, 1987; Bouchard et al., 1990; Hirvas et al., 1995). These deposits are overlain by patches of glaciofluvial sand and gravel deposits (Repo et al., 1970; Haavisto-Hyvärinen et al., 1996). Within basin areas, these deposits show up to 15 m thicknesses (Haavisto and Kukkonen, 1975; Haavisto-Hyvärinen et al., 1996), which suggests their preservation and low erosion during the last deglaciation.

The Helsinki-Espoo coastal area has undergone several Baltic Sea phases after the last deglaciation from 13,000 years ago to present day sea level (Björck, 1995; Stroeven et al., 2016; Andrén et al., 2000). During the repeated marine and lacustrine phases, fine-grained sediments were deposited as infills of distinct topographical depressions but also as thinner units with wide spatial coverage. When the Helsinki-Espoo coastal areas eventually emerged from the sea due to the post-glacial land uplift (Donner, 1995), the sea currents and littoral processes washed and partly redeposited the fine-grained clays and silts and, subsequently, the underlying till and glaciofluvial deposits which led to the exposure of the crystalline bedrock at the hilltops and resorted littoral deposits on the hill slopes (Fig. 3; Repo et al., 1970; Haavisto and Kukkonen, 1975).

The basal tills characteristically appear on the distal side of elevated areas and as infills of basin-shaped features (Evans et al., 2006). The

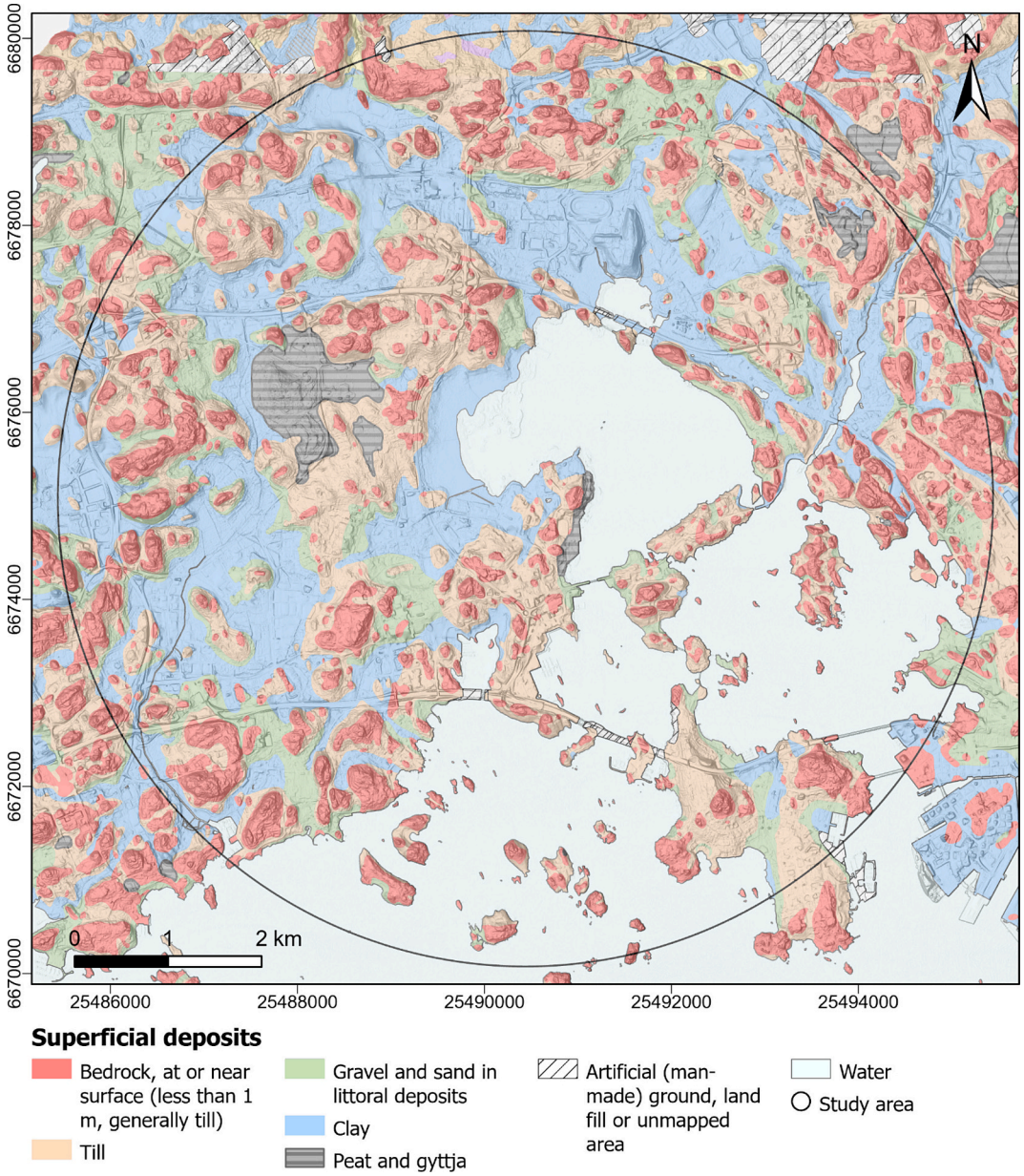

Fig. 3. Superficial deposits map of the study area (Superficial deposits 1:100000, 2015; Superficial deposits 1:20000, 2015 © Geological Survey of Finland). Multidirectional hillshade generated using LiDAR data (Laser scanning data 0,5 p, 2008-2019 © National Land Survey of Finland; hereafter NLS).

clast fabric orientations determined from the local tills and the striations recorded from bedrock outcrops indicate the Pleistocene ice sheets have advanced over the study area from NW and N (Repo et al., 1970; Rainio and Lahermo, 1976; Hirvas and Nenonen, 1987; Hirvas et al., 1995). Therefore, the potential location of thick till deposits within our study area can be expected in linear bedrock surface depressions that trend NE and E; i.e. perpendicular to the prevalent ice flow directions. Finally, Repo et al. (1970) have documented up to 20–30 m thick till beds localized in narrow shaped and deep bedrock surface depressions in Espoo area, few kilometers west from the study area.

3. Data and methods

We began with 2D analysis of bedrock ductile structures and deformation zones from geological and geophysical datasets and correlated the resulted 2D lineaments with the linear topographic depressions recognized from the conventional bedrock-DEM generated from bedrock surface elevation points (Fig. 4). Subsequently, we determined the thickness of the overburden occurring within the deformation zones and used this information to generate an improved version of the bedrock-DEM. Finally, we used the resulting models to create thickness maps of i) the LBS, and ii) the overburden. For the 3D model building and structural analysis, we used MOVE™ from Petroleum Experts and Leapfrog Geo™ from Bentley Systems. The coordinates in all figures are presented in ETRS89 / GK25FIN (EPSG:3879).

3.1. 2D structural analysis

We conducted a form line interpretation of the regional-scale patterns of ductile deformation from foliation data (Foliation observations, n.d., 1867 points in Fig. 7A), regional lithologic map (modified after Bedrock of Finland 1:200000, 2022; Fig. 7A), and aeromagnetic map (modified after Aeromagnetic anomaly map of Finland, 1972–2007; Fig. 7B) with the aim to understand pre-existing structures, which potentially control the location and geometry of brittle deformation zones (e.g. Stephens et al., 2015; Skyttä and Torvela, 2018). We made

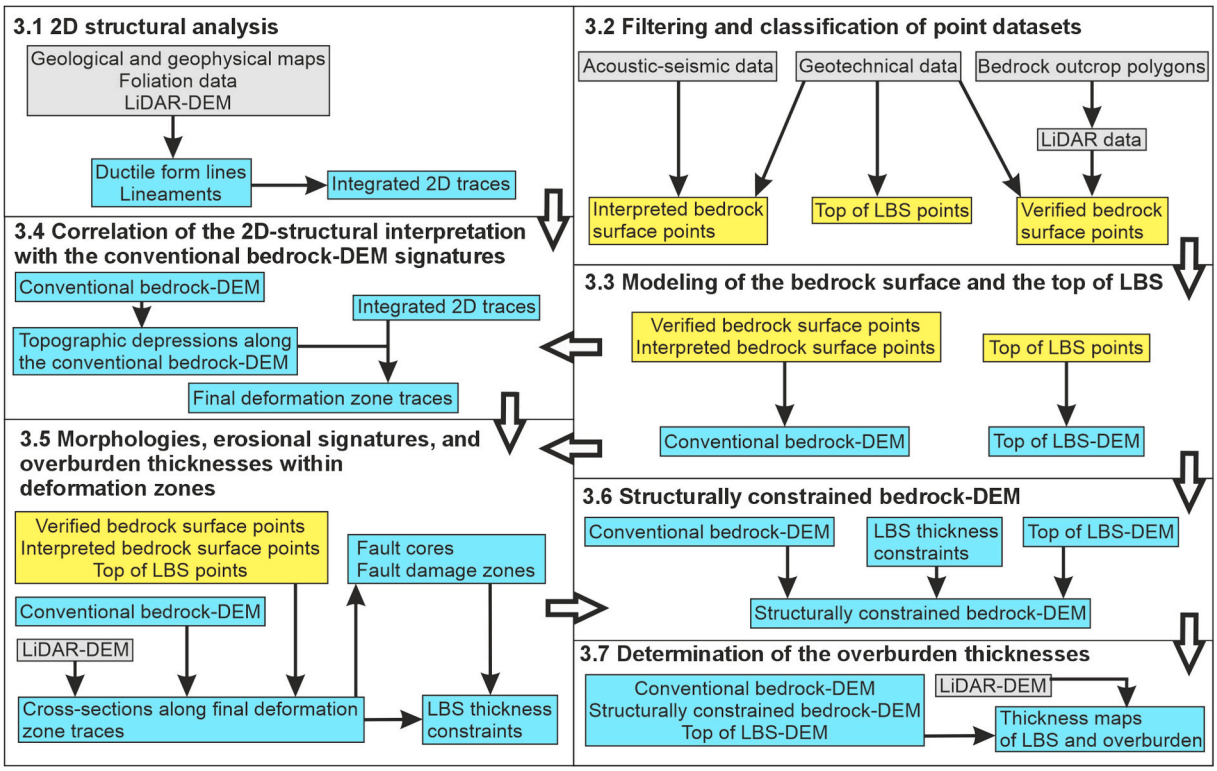

Fig. 4. Workflow diagram highlighting the source datasets (grey), the processed datasets (yellow), and the main results/outcomes (light blue) of each step. The thin arrows indicate analysis/processing in each step whereas the thick arrows indicate the use of the generated models in following steps. The bolded headings correspond to the sections in this paper for detailed descriptions. (For interpretation of the references to colour in this figure legend, the reader is referred to the web version of this article.)

the first interpretation using the foliation data and the regional lithological map (Fig. 7A), which we subsequently modified using the continuous patterns in the aeromagnetic map (Fig. 7B). The ductile form lines aimed at visualizing the overall structural trends, linear ductile zones characterized by distinct changes in foliation strikes, and internally homogeneous structural domains, which are typically bound by the ductile shear zones (Fig. 7A). Subsequently, we conducted a lineament interpretation of linear discontinuities within the foliation, magnetic and topographic data (Figs. 7A, B, C), which ideally represent zones of brittle deformation. Finally, we compared the interpretations of the ductile form lines and lineaments and classified the resulted traces into two classes based on their geological character and length (Fig. 7D).

3.2. *Filtering and classification of point datasets*

We extracted bedrock surface elevation data points from geotechnical data (Geotechnical ground investigations-a, n.d., Geotechnical ground investigations-b, n.d.; Figs. 5A–B), LiDAR-DEM (Elevation model 2 m, n.d.; Fig. 5A), and acoustic-seismic data from the marine areas (Acoustic-seismic sub-bottom profiling data, n.d.; Fig. 5B) to generate a conventional bedrock-DEM representing the partially exposed bedrock surface (Fig. 8). We digitized the boundaries of exposed bedrock outcrops from the Map of Quaternary Deposits for City of Espoo (Espoo, 1986) and Soil and Base maps for City of Helsinki (Helsinki, 2017, 2019) and extracted the LiDAR data points from those areas at 10 m horizontal spacing, resulting in 151925 *verified LiDAR bedrock surface points* (Fig. 5A).

For modeling the unexposed parts of the bedrock, we had access to a total of 87,428 geotechnical ground investigation data points, out of which 28,828 are classified as *verified geotechnical bedrock surface points* as their ending against the bedrock surface has been reliably verified by the applied method (Fig. 5; percussion drilling, MW-drilling, casing, or test pits; terms after European Committee for Standardization (CEN, 2007)). The remaining geotechnical data points (n = 58,600) were classified as the *top of LBS points* which we derived from those geotechnical ground investigations that terminated against a boulder, bedrock surface or a dense sedimentary layer, or between boulders (Fig. 5D; percussion drilling, weight sounding test, casing, static dynamic penetration test, hammer drilling, dynamic probing, vibration drilling). In this study, the concept of LBS includes roughly the basal till, gravel, and sand units (Fig. 5D) against which majority of the geotechnical drillings have terminated for engineering reasons (e.g. Hanna et al., 2022). Therefore, it is more of a general concept than individual sedimentary layers.

To complement the sparse and unevenly distributed verified geotechnical bedrock surface points (Fig. 5A), we generated the *interpreted geotechnical bedrock surface points* using the top of LBS points by lowering their elevation by one meter, which is considered as the minimum thickness of the eroded layer beneath an ice sheet consisting of subglacial debris (Eyles et al., 2016). Using a triangular irregular network (TIN) surface generated from the verified LiDAR and verified geotechnical bedrock surface points only, we further filtered out those interpreted points that overlie the TIN and retained those that underlie the TIN (Fig. 5C). The purpose of the filtering is to exclude those points that likely represent LBS and not the bedrock surface. Input dataset for the build-up of the conventional bedrock-DEM further comprises the *interpreted acoustic-seismic bedrock surface points* (n = 11,313) from the marine areas, which have been derived from 90 km of acoustic-seismic sub-bottom profiling surveys. The method includes combination of low and high frequency echo sounder, and single channel reflection seismic profiling with +/− 2 m resolution without in situ verification of the bedrock surface (Virtasalo et al., 2019).

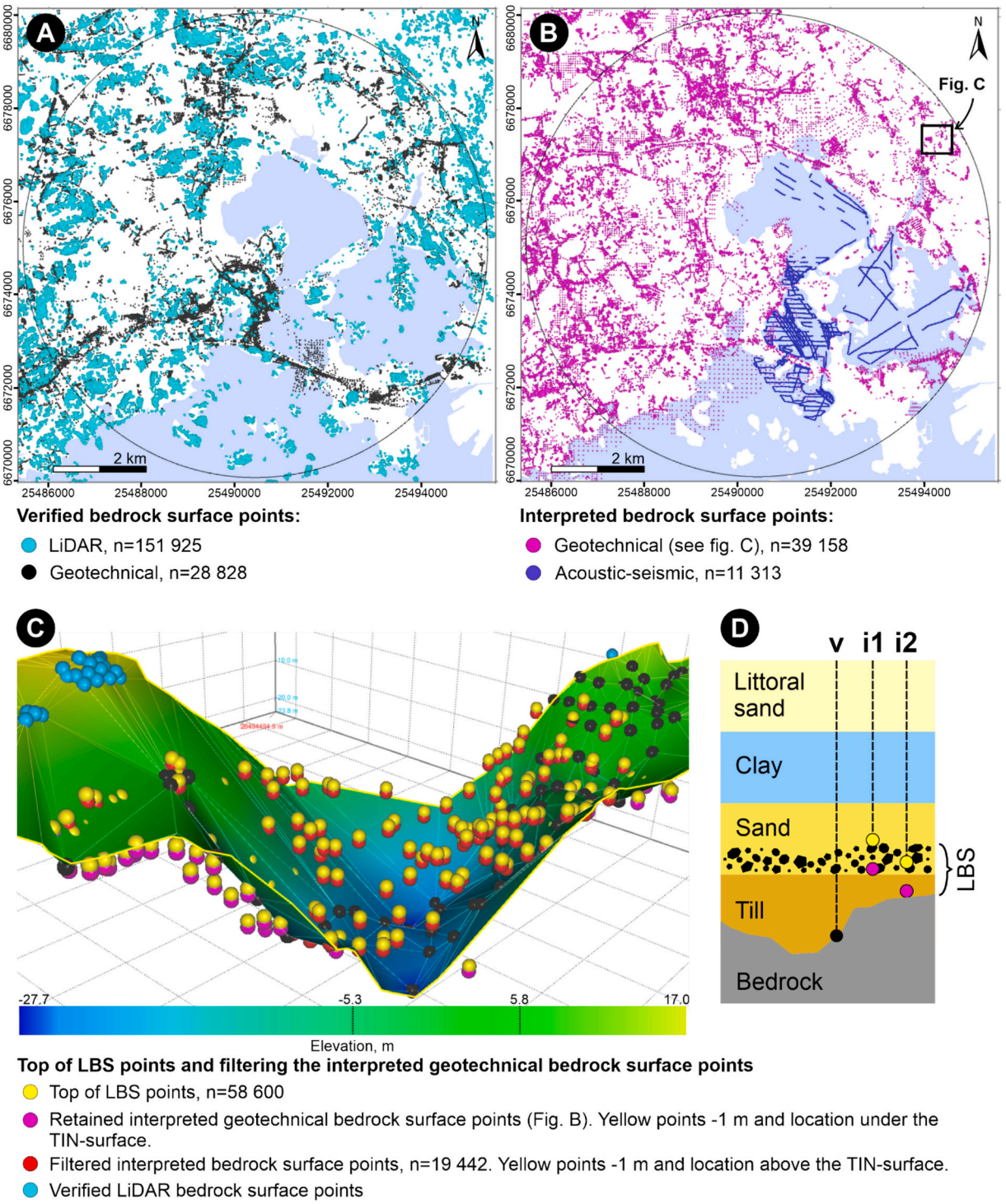

Fig. 5. Spatial distribution of the input data points used in modeling. A) The verified and B) the interpreted bedrock surface points. The marine area is highlighted with the blue polygon. C) A slice of the TIN-surface used in filtering of the interpreted geotechnical bedrock surface points. 4× vertical scaling. D) Stratigraphy of the superficial deposits and the concept of LBS. Black dot in geotechnical borehole *v* illustrates a verified geotechnical bedrock surface point. Boreholes i1 and i2 lack verification of bedrock surface and have terminated against the LBS at slightly different depths. (For interpretation of the references to colour in this figure legend, the reader is referred to the web version of this article.)

3.3. Modeling of the bedrock surface and the top of LBS

We interpolated the conventional bedrock-DEM (Fig. 8) by using the verified (geotechnical and LiDAR; $n = 180{,}753$; Fig. 5A) and the interpreted (geotechnical and acoustic-seismic; $n = 50{,}471$; Fig. 5B) bedrock surface points. We used the Ordinary Kriging interpolation method (e.g. Davis, 2002), as it can be optimized to highlight the spatially continuous linear valleys attributed to the bedrock deformation zones. We used 30 m × 30 m grid cells and "honor points" -setting not to overemphasize the smoothness of the kriging interpolation. Furthermore, we iterated the associated semivariogram to achieve the best fit between the experimental variogram illustrating our point dataset and the geostatistical variogram models (Davis, 2002). As a result, we used the exponential variogram model with the following values: Partial sill = 155, Range =

2400 m, Max lag distance = 4800 m, number of lags = 20, and tolerance = 30 m. As a reference surface in improving the bedrock-DEM (Section 3.6), we also interpolated a top of LBS-DEM by using the top of LBS points (n = 58,600; Fig. 5C). We used 40 m × 40 m grid cells without "honor points" -setting as the top of LBS is likely a sub-horizontal surface and no GIFs that would have led to abrupt changes in the LBS topography have been recognized in the study area (Sutinen et al., 2021). The spherical variogram model showed the best fit for the top of LBS points, using Partial sill = 95, Range = 1500 m, Max lag distance = 4000 m, number of lags = 25, and tolerance = 30 m values.

3.4. Correlation of the 2D-structural interpretation with the conventional bedrock-DEM signatures

We delineated distinct linear topographic depressions from the conventional bedrock-DEM (Figs. 8, 9A) and correlated them with the deformation zone traces recognized from the 2D-structural analysis (Section 3.1; Fig. 9B). The result of the correlation are *the final deformation zone traces* (Fig. 9C), which contain also trace lines of those topographic depressions that were not distinguishable from the 2D datasets. The correlation aimed at decreasing the uncertainty associated with the lateral continuity of the bedrock depressions, which may be limited by the coverage of the bedrock surface points, while the corresponding geological structures may be more continuous or discontinuous. Furthermore, the correlation also verified which of the depressions are associated with deformation zones rather than represent e.g. lithologies that are undeformed but prone to glacial erosion. The correlation steps involved extending, joining, and straightening the depression traces based on the 2D traces in areas with very limited coverage of bedrock surface points. We classified each final deformation zone trace (Sections 4.3, 4.4) as major, intermediate, or minor based on their length and topological relationship. The minor zones abut against or cross the intermediate or the major zones and the intermediate zones abut against or cross the major zones, which are the longest ones.

3.5. Morphologies, erosional signatures, and overburden thicknesses within deformation zones

We created a series of cross-sections across diverse deformation zones (Section 3.4) at locations that have the best available coverage of both the verified bedrock surface points and the top of LBS points (Figs. 5A, 9D). We projected the verified and interpreted bedrock surface points, and the top of LBS points to the sections perpendicularly from both sides of the section with a maximum distance of 25 m. From these sections, we recognized abrupt changes in the elevation level of the verified bedrock surface points, which we attributed to the presence of sub-vertical faults or fractures (Elminen et al., 2008; Wennerström et al., 2008), and re-interpreted the conventional bedrock-DEM intersection to better reflect the fracture-controlled, stair-stepping morphology of the bedrock surface (Fig. 10; App. A). We interpreted the stair-stepping morphology only in those sections that show more than one verified bedrock surface point within the sub-surface. When applicable, we further assigned the distinct narrow depressions in the central parts of the depressions to fault cores and made a rough delineation of the surrounding damage zones. We measured the thickness of the LBS both above the fault cores and the damage zones as the vertical separation between the projected verified bedrock surface points and the projected top of LBS points. Furthermore, we created a set of cross-sections outside the deformation zones (Fig. 10F; App. A) for the comparison of the overburden and the LBS thicknesses between the topographic depressions and other areas.

3.6. Structurally constrained bedrock-DEM

We improved the reliability of the conventional bedrock-DEM through modifying it to honor the new constraints about the LBS thicknesses within the deformation zone-controlled bedrock surface depressions (Sections 3.5; 4.4; 4.5). The modification involved projecting the final deformation zone traces onto the LBS-DEM (V in Fig. 6B) and further downward adjustment of their vertical position (VI and VII in Fig. 6B) based on the observed maximum LBS thickness values for the deformation zones: −19 m, −11 m, and − 5 m for the major, intermediate, and minor zones, respectively (Figs. 10B–E). We used the LBS-DEM as the reference surface as it is based on much denser and spatially uniform point data than the conventional bedrock-DEM, and hence results in a reliable elevation reference. The adjusted traces were manually edited to snap on the conventional bedrock-DEM in locations where the elevation of the conventional bedrock-DEM was lower than the adjusted traces and their depth was progressively reduced to 0 m at the terminations of the depressions. Finally, we pulled the conventional bedrock-DEM down to the adjusted deformation zone traces (IX in Fig. 6C) by using the "pull to line" tool in MOVE™ with the sines interpolation (0, pi/2) setting as the across geometry of the resulted depressions. The modification was laterally limited into a uniform width using 150 m, 70 m, and 50 m width for the major, intermediate, and minor zones to reflect the observed widths of the respective ground surface depressions (II in Fig. 6A). The resulting *structurally constrained bedrock-DEM* (X in Fig. 6C) provides an improved spatial representativity of the topographic depressions with respect to both their depth and lateral continuity.

3.7. Determination of the overburden thicknesses

We calculated and visualized the thickness of the LBS and the overburden separately by using the bedrock-DEMs (the conventional and the structurally constrained one), the LBS-DEM and the LiDAR-DEM (Elevation model 2 m, n.d.) as the reference surfaces (Figs. 11A–D). For the reference in marine areas, we used seabed elevation data points (Topographic database), offshore geotechnical data (Geotechnical ground investigations-a, n.d., Geotechnical ground investigations-b, n.d.; Fig. 5B), and the acoustic-seismic data (Acoustic-seismic sub-bottom profiling data, n.d.; Fig. 5B).

4. Results

4.1. Preliminary interpretation of ductile structures and deformation zones

Based on the 2D structural analysis, the bedrock structures within the study area are characterized by folds with sub-vertical axial surfaces trending E, and the overall foliation orientations are dominated by sub-vertical attitudes with a wide overall scatter in trends, while a clear maximum corresponding to ENE trend is present (Fig. 7A). The most apparent areas of localized strain occur in the north where the foliation pattern indicates an E trending domain characterized by a dextral SC-structure (purple lines in Fig. 7A) and, towards south, an adjacent E trending domain with isoclinal folds (magenta lines in Fig. 7A). A deformation zone along the southern margin of the isoclinally folded domain (southern black line II in Fig. 7A) terminates in the east where the folding pattern changes from isoclinal to more open towards SE, where an abrupt change in foliation trend indicates the presence of a NE trending deformation zone along the fold limb (III in Fig. 7A). The central and southern study areas are characterized by overall lower strain in comparison with the northern areas, and their structural geometry is dominated by a large open '*Z*-shaped' fold with an approximately 2 km amplitude (blue lines in Fig. 7A). Deformation zones within the central and southern areas trend ESE and NE and are located along the limbs of the major folds (IV and V in Fig. 7A). The south-western study area comprises domains of NE trending foliations (red lines in Fig. 7A) and an elliptically shaped lithologic unit (orange lines in Fig. 7A), and folds with tight geometry characterized by NNE trending axial surfaces and 200 m amplitudes (yellow lines in Fig. 7A).

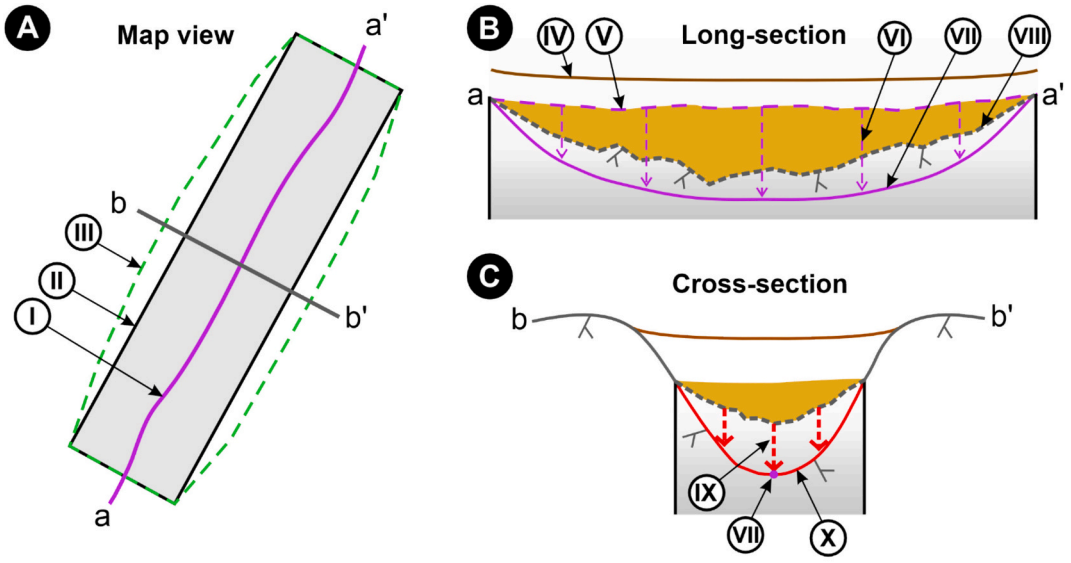

Fig. 6. Schematic presentation of improving the conventional bedrock-DEM based on the measured LBS thicknesses. A) Map view showing the bedrock surface depression area and the associated DEM modification area. B) Methodology of adjusting the vertical position of the deformation zone traces. C) Methodology of pulling the conventional bedrock-DEM to the adjusted deformation zone traces resulting in the structurally constrained bedrock-DEM.

4.2. Integrated 2D ductile structures and deformation zones

The ductile domains recognized from the geological datasets are also distinguishable from the aeromagnetic map (Fig. 7A–B). Correlation of the ductile form lines with the aeromagnetic map and ground surface LiDAR-DEM resulted in modifications to the line geometries and intensities in all domains.

The preliminary E trending deformation zone I in the north (Fig. 7A) continues through the study area both on the aeromagnetic map and the LiDAR-DEM, both showing further parallel zones within the eastern part of the zone (I in Fig. 7B–C). Towards south, the preliminary E trending deformation zones II (Fig. 7A) along both margins of the isoclinally folded ductile domain (magenta lines in Fig. 7A) show approaching geometric relationship in the east where they abut against shorter NNW trending magnetic lineaments, which in turn abut against the largest E trending zone in the north (Fig. 7B). Similar to Zone I, the southern margin of the isoclinally folded domain is not an individual feature but comprises another parallel E trending zone on the aeromagnetic map (II in Fig. 7B), where the LiDAR topographic lineament is also the most pronounced (II in Fig. 7C).

The NNE trending preliminary deformation zone III in the northeast has a very limited length of 2.5 km as based on the foliation data (Fig. 7A). However, this zone is more continuous within magnetic and, and particularly the LiDAR datasets, and was therefore extended across the whole study area towards SSW (Figs. 7B, C). This major discontinuity has a minimum length of ca. 12 km, extending beyond the studied area. In the north, several shorter NNW trending lineaments abut both against this deformation zone and the E trending zones in the north, apparently linking the two most distinct deformation zones within the study area (Fig. 7B). To the southeast of the NNE trending major zone, a parallel but shorter lineament is visible within the magnetic data, but not within the other 2D datasets, and hence this shorter lineament is not included in the integrated lineaments.

The ESE trending deformation zone occurring along the northeastern limb of the Z-shaped fold (IV in Fig. 7A) abut against the E trending deformation zone II in the preliminary interpretation but displays a cross-cutting geometry and westward continuity along the axial surface of the isoclinal folds in the magnetic, and particularly the LiDAR data (IV in Figs. 7B and C). Towards east, zone IV terminates against the NE trending deformation zone III in magnetic data but shows cross-cutting character on LiDAR-DEM (Figs. 7B and C). On the LiDAR-DEM, several small NNW trending deformation zones are present within the area of intersection between the zones III and IV.

The preliminary NE trending deformation zone along the southwestern limb of the Z-shaped fold (V in Fig. 7A) shows multiple parallel segments on the aeromagnetic map, while LiDAR-DEM displays some additional NNE trending lineaments, which abut against the more dominant NE trending zones (V in Figs. 7B-C).

As a result of integrating the lineaments from different sources (Figs. 7A-C), the interpretated deformation zones comprise the following major zones: E trending deformation zones in the north (I and II), the NE trending deformation zone in the southeast (III), and the ESE trending deformation zone in the middle of the study area (IV). The remaining lineaments are classified as minor deformation zones, which may be either independent, or spatially associated with the major zones with splay-like geometries (dashes lines in Fig. 7D).

4.3. Conventional bedrock-DEM and the final deformation zone traces

The conventional bedrock-DEM is characterized by variably discontinuous elongate topographic depressions throughout the area, and more equant-shaped, wider topographic lows localized especially at the center and southern study areas (Fig. 8). The elongate depressions have dominant ENE and NW trends, but the overall scatter is wide.

The NE trending depression in the eastern study area (NE in Fig. 8) is the most significant elongate depression along the bedrock-DEM as it has a significant depth and lateral continuity, and it constraints the length of many of the other (abutting) depressions.

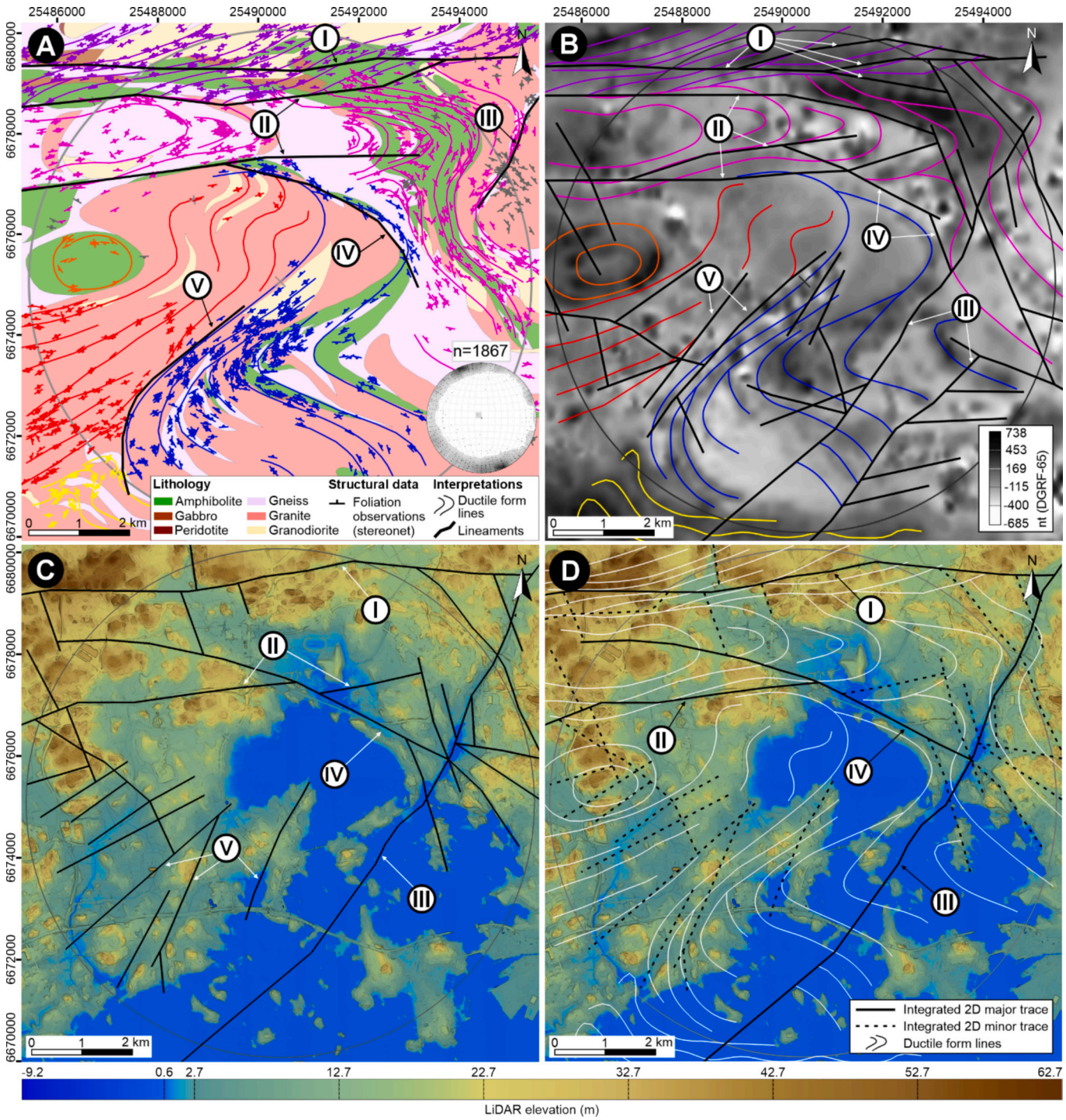

Fig. 7. 2D interpretation of the ductile structures and the deformation zones. A) Ductile form lines developed from foliation data (Foliation observations, n.d) and regional lithological map (modified after Bedrock of Finland 1:200000, 2022 © GTK). The black lineaments stand for discontinuities recognized from abrupt changes in foliation patterns. B) The ductile form lines and lineaments modified based on the aeromagnetic map (modified after Aeromagnetic anomaly map of Finland, 1972–2007 © GTK). C) Modification of the lineaments along the LiDAR DEM (Elevation model 2 m, n.d. © NLS). D) The 2D-deformation zone interpretation based on the integration of the lineaments in A-C. The study area shown as the grey circle.

The northern study area shows E trending topographic depressions (E in Fig. 8) with shorter NNW and NNE trending depressions that abut the E trending ones. Towards south, the NNW and NNE trending depressions link the *E*-trending depression to the ESE trending depressions (ESE in Fig. 8) that continue as segments through the study area and abut the NE trending depression in the eastern study area. The easternmost ESE trending segment shows a short E trending splay. In the north-west, the NNE trending depressions continue further south and link the previous zones with another set of E-trending depressions (E2 in Fig. 8).

The western and south-western study areas are characterized by orthogonal set of depressions that show NW and NE trends, and the south-eastern study area shows an orthogonal set of depressions with ENE and NNW trends.

Approximately half of the depressions correlate spatially with the integrated 2D traces whereas the other half were only distinguishable

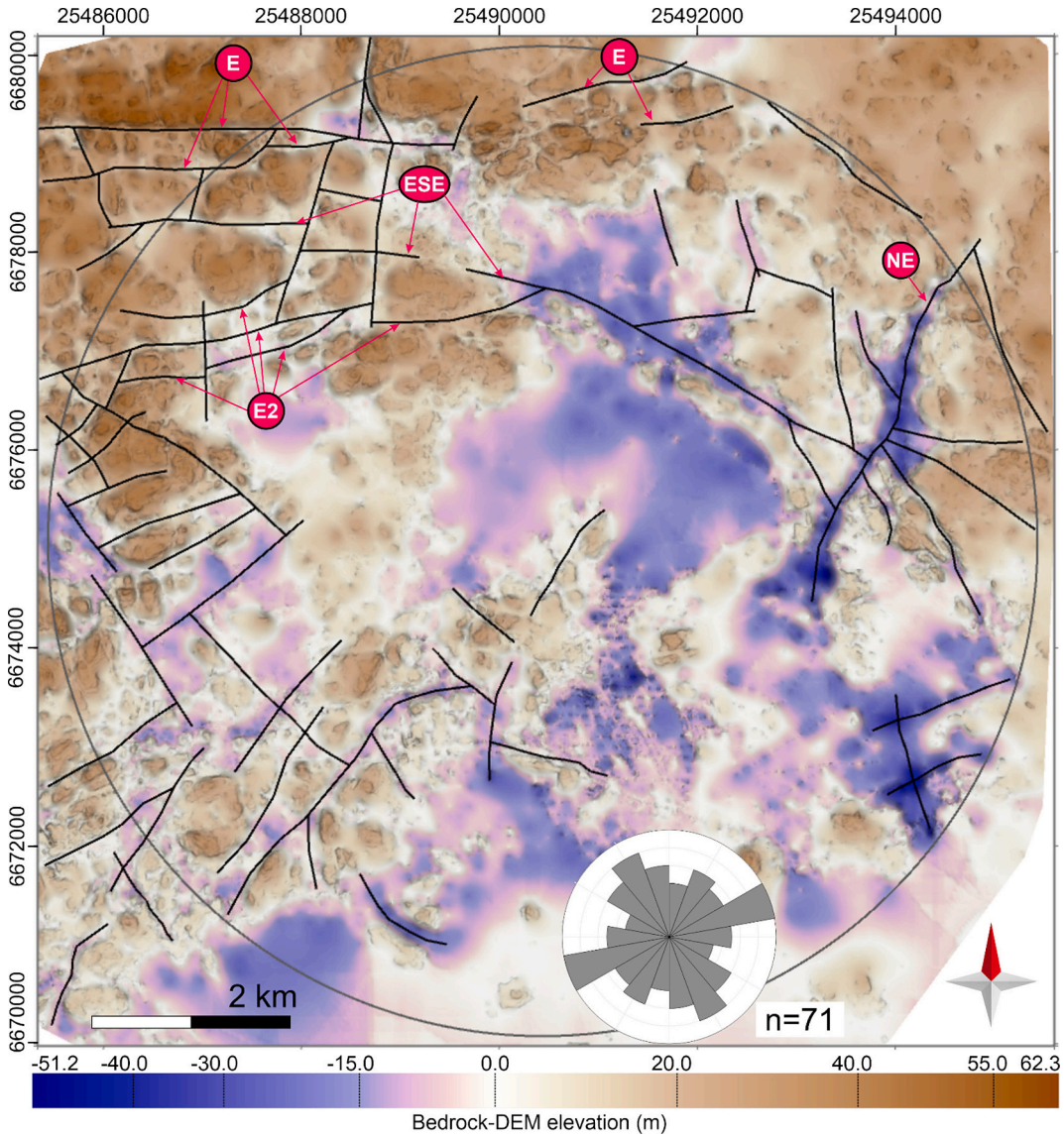

Fig. 8. Digital elevation model of the partially exposed erosion surface of the bedrock as generated within this investigation. The DEM is overlain by an interpretation of linear topographic depressions. 4 x vertical scaling.

from the bedrock-DEM (Figs. 9A, B). After correlating the depressions with the integrated 2D traces and classifying them based on their length and topology (section 3.4, Fig. 9B), we identified three major final deformation zone traces (F1-F3 in Fig. 9C) and several associated intermediate and minor final deformation zone traces.

The E trending F1 continues through the study area in the north and shows subparallel intermediate splays, an abutting N trending intermediate trace, and several abutting NNW and NNE trending minor traces in the northwest (Fig. 9C). In the northeast, the F1 and F3 are linked by abutting NW trending intermediate traces.

Towards south, the F2 is an E to ESE trending feature which terminates in isolation in the west and abuts the F3 in the east (Fig. 9C). The F2 shows crossing N to NNE trending intermediate traces in the west that link it to the F1. At the center, the F2 shows two E trending splays of which the western one is significantly longer than the eastern one. The F2 abuts the F3 in the east (Fig. 9C).

The NE trending F3 terminates in isolation in the southwest and continues northeast out from the study area (Fig. 9C). The F3 shows several abutting intermediate traces and few minor traces concentrated on the middle of the zone (Fig. 9C).

In addition, the western and south-western study areas are characterized by NE and NW trending intermediate traces, and the south-eastern study area shows a set of ENE and NNW trending intermediate traces.

4.4. Morphologic signatures of the bedrock surface and thickness of the LBS and the overburden

The largest observed abrupt change in elevation of the bedrock surface from the host rock into the deformation zone is approximately 30 m (Figs. 10 A-B and App. A) within the major final deformation zones. The bedrock surface shows either symmetrical (e.g. sections M1, M3 in App. A) or asymmetrical (e.g. sections M6, M7 in Figs. 10 A-B; and M2, M8 in App. A) cross profiles. The overburden and the LBS show maximum thicknesses of >30 m (Figs. 10 A-B) and 19 m (Fig. 10B), respectively, and they are located above the topographic minimums of the bedrock surface which possibly correspond to the cores of the deformation zones.

Within the influence of the intermediate final deformation zones, the maximum abrupt drop in the elevation of the bedrock surface is 20–30 m (Figs. 10C–D) and the bedrock surface shows symmetrical cross-profile in all the sections (I3 and I4 in Figs. 10C-D; I1 and I2 in App. A). The

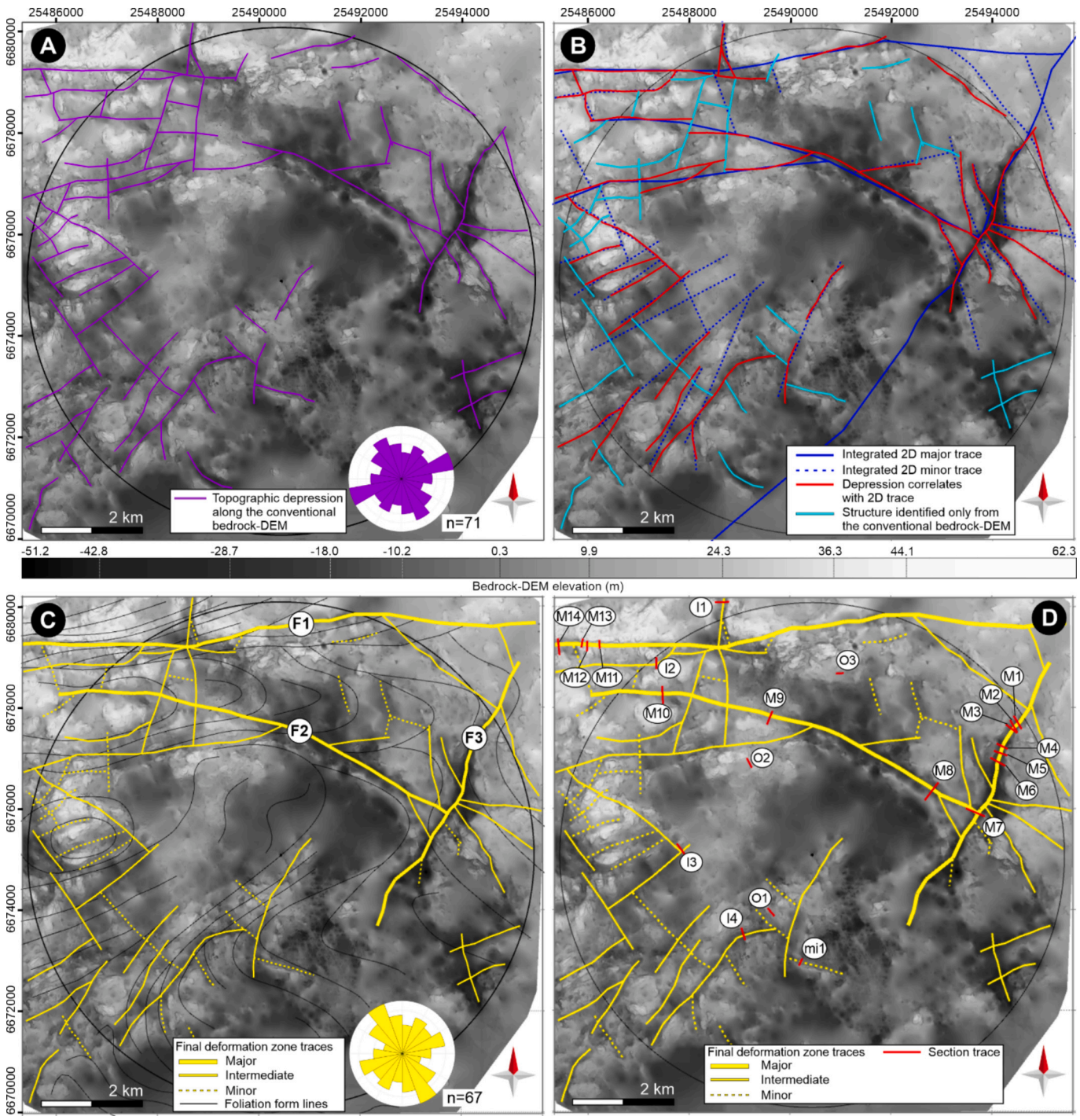

Fig. 9. A) Elongate topographic depressions along the conventional bedrock-DEM. B) Correlation of the depressions with the integrated 2D deformation zone traces. C) The final deformation zone traces resulted from the correlation and classification process. D) The locations of the cross-sections for analysis of the erosional signatures of the deformation zones and the LBS and overburden thicknesses (next section). 4× vertical scaling in A-D.

overburden and the LBS show maximum thicknesses of 15–20 m and 11 m, respectively. Only the cross-section I4 (Fig. 10D) contains enough source data points for the interpretation of the fault architecture.

The minor final deformation zones show the maximum of 15 m in abrupt decrease of the bedrock surface elevation (Fig. 10E). The overburden and the LBS show maximum thicknesses of 10 m and 5 m, respectively (Fig. 10E).

The sections that are located outside the influence of the deformation zones show an overall flat topography of the bedrock surface with no distinct topographic depressions (O3 in Fig. 10F; O1, O2 in App. A). These sections show the maximum overburden and LBS thicknesses of 5 m and 3 m, respectively (Fig. 10F).

4.5. Overburden and LBS thickness maps

Using the conventional bedrock-DEM in calculations, slightly more than half of the ground surface area is covered by 0–5 m, and 25 % of the area by 5–10 m thick overburden that occur within scattered basins of variable sizes and shapes (Fig. 11A). As the thickness increases (>10 m), some major basins are still present, such as the one in the middle of the

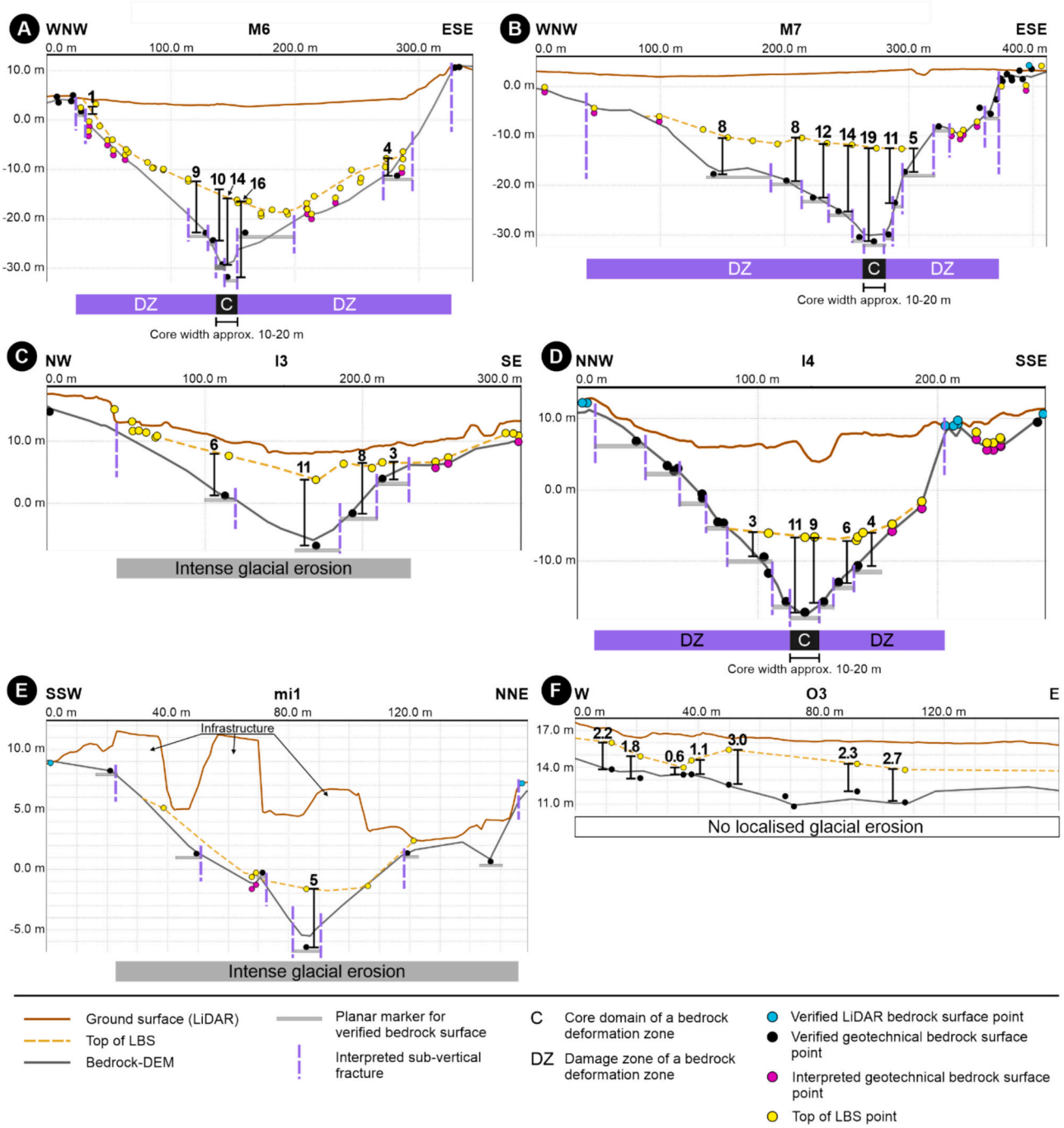

Fig. 10. A selection of cross-sections across the bedrock deformation zones (A-E) and outside their influence (F) in locations with the best available coverage of the source data points. The maximum thickness of LBS within the major, intermediate, and minor deformation zones are 19 m (B), 11 m (D), and 5 m (E), respectively. The LBS thickness outside the deformation zones varies between 0.6 and 3 m (F). The Section ID is given above the image and their locations are shown in Fig. 8D. All the sections indicated in 8D are shown in App. A. 4× vertical scaling in A-F.

study area (Fig. 11A), but these thicker deposits preferably define narrow elongate geometries with significant lateral continuities. The areas of maximum overburden thicknesses (>20 m) cover about 2 % of the ground surface area and they are spatially associated with the linear bedrock surface depressions, which corresponding to the major deformation zones (Figs. 9C, 11A). By using the ***structurally constrained bedrock-DEM*** as the bedrock surface reference (Fig. 11B), the overall distribution of the overburden thickness is approximately the same for the thickness ranges between 0 and 20 m (Figs. 11A-B), but the thickest deposits (>20 m) show more continuous shapes and their ground surface area is doubled to approximately 4 % (Fig. 11B).

The LBS deposits are dominated by up to 1 m thick deposits including areas with no LBS (Fig. 11C). The 1–3 m thick LBS deposits cover about 20 % of the area and they show scattered basins of variable size and irregular shapes. The >3 m thick LBS deposits show significantly less areal coverage than the <3 m thick deposits as they cover only about 11 % of the area. The thickest LBS deposits (> 13 m) are focused on the central and eastern study area with the thickness maximum localized within the NE- trending F3 zone (Figs. 9C, 11C). By using the structurally constrained bedrock-DEM as the reference of the bedrock surface, the spatial distribution of the up to 3 m thick LBS deposits stays about the same (Figs. 11C-D) whereas the thickest LBS deposits are more

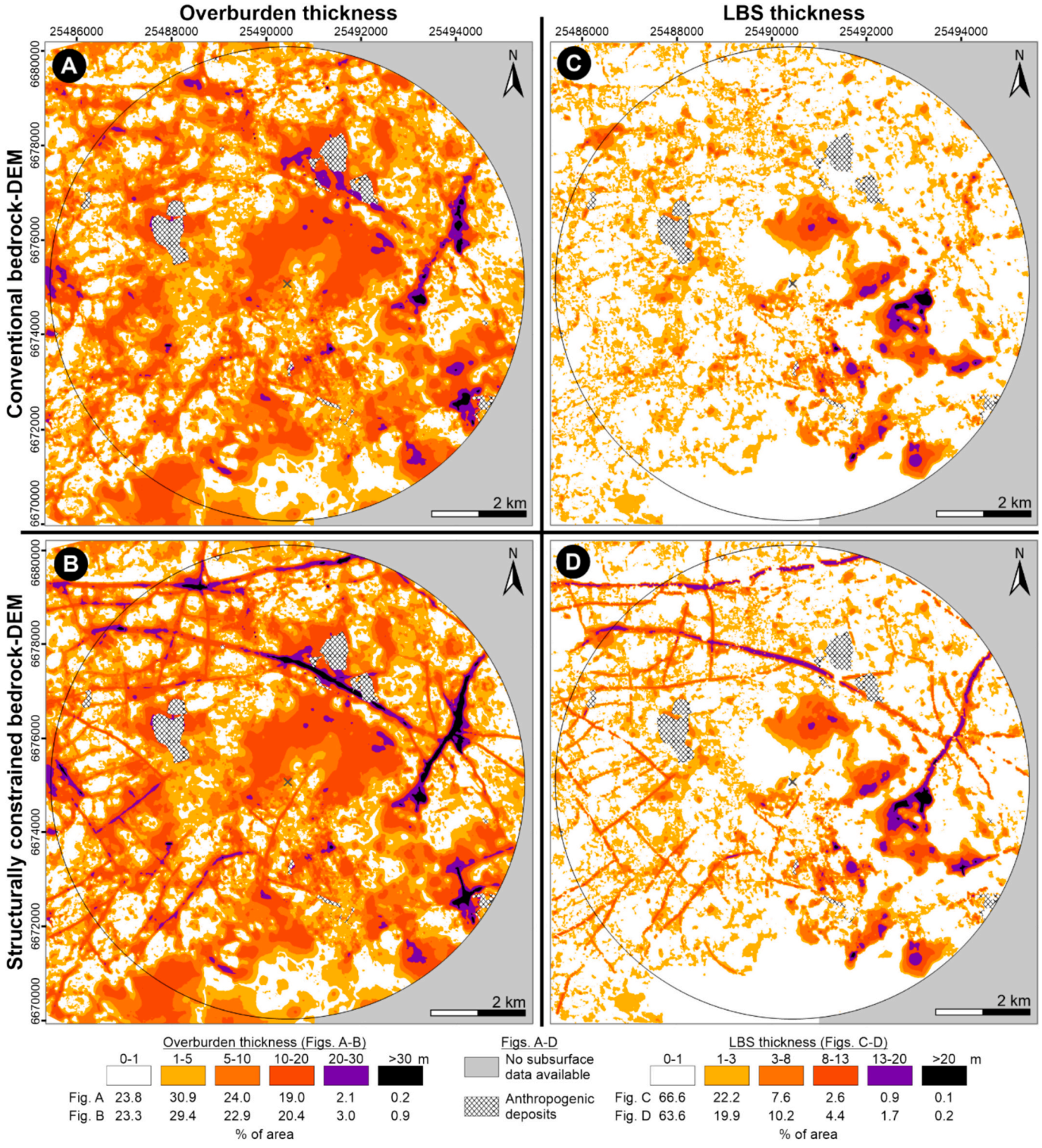

Fig. 11. Thickness maps of the overburden (A-B) and the LBS (C–D). The thickness of the overburden visualized as the vertical separation between A) the bedrock-DEM and the LiDAR-DEM (Elevation model 2 m, n.d. © NLS), and B) the structurally constrained bedrock-DEM and the LiDAR-DEM. The thickness of the LBS visualized as the vertical separation between C) the conventional bedrock-DEM and the LBS-DEM, and D) the structurally constrained bedrock-DEM and the LBS-DEM. Significantly thick anthropogenic deposits (e.g. landfills) shown as crossed areas.

clearly localized on top of the bedrock deformation zones (Fig. 11D).

5. Discussion

The extensive geotechnical dataset ($n = 87{,}428$; Fig. 5) merged from various sources and further used in the model building in this study provides a robust dataset for modeling the topography of the bedrock erosion surface in unexposed areas (Figs. 8–10), and the spatial distribution and thickness variations of the overlying LBS and overburden (Fig. 11). However, the uncertainties in the representativeness of the geotechnical data resulted in discontinuous topographic depressions along the conventional bedrock-DEM (Fig. 8) and thereby the thickness

estimates of the overburden using the conventional bedrock-DEM as the basement surface are likely too low. The uncertainties stem from the uneven spatial distribution of the data, and particularly the limited availability of verified bedrock surface points within areas where the bedrock deformation zones have controlled the glacial erosion. To rectify the problem, we modified the conventional bedrock-DEM based on the measured LBS thicknesses known from well-characterized deformation zones, and our deformation zone network interpretations. The resulted structurally constrained bedrock-DEM honors the presumed continuity of the deformation zones and can be used as geologically justified reference in evaluating the thicknesses of the LBS and overburden.

5.1. Representativeness of the geotechnical data

To improve the overall coverage of the geotechnical bedrock surface points in the unexposed areas, we generated the supplementary dataset "*interpreted geotechnical bedrock surface points*" from the top of LBS points. The supplementation resulted in an increase of input data points from 28,828 to 67,986 (Fig. 5), and consequently significantly improved the spatial coverage of the data. The applied subtraction of one meter is rather conservative as our LBS thickness analyses from the areas outside the bedrock deformation zones (O3 in Fig. 10F; O1 and O2 in App. A) indicate that LBS thicknesses locally extend up to 3 m. This may be due to the uneven character of the bedrock surface morphology even outside the bedrock deformation zones, which is likely controlled by the heterogeneity in the occurrence of the sub-vertical fractures (Wennerström et al., 2008), or the contrasting deposition of subglacial sediments on the proximal vs. distal side of the elevated areas (e.g. Alley et al., 2021). Consequently, the natural variation in the LBS thickness causes an uncertainty of two meters in the vertical position of the modeled surface of the eroded bedrock, which in the regional approach is insignificant for most applications.

By contrast, the thickness analyses across the bedrock deformation zones clearly indicate LBS thicknesses greatly exceeding the aforementioned 1–3 m values (Fig. 10 A–E), for which reason the interpreted geotechnical bedrock surface points located within the bedrock deformation zones are likely to have too high elevation values. Our analysis indicated a maximum LBS thickness of 19 m (Fig. 10B) for the largest depressions (and deformation zones) which is in line with the earlier studies pointing up to 20–30 m thick successions of coarse sediments along such depressions (Repo et al., 1970). Filtering of the interpreted geotechnical bedrock surface points occurring within the bedrock deformation zones (Section 3.2) may have removed some points that indicate the true bedrock surface, but it was necessary as the too high elevation values of the interpreted points used together with the verified points would have led to zig-zag shapes along the generated bedrock-DEM and too high elevation values for the deepest bottoms of the linear topographic depressions. Furthermore, there may be significant local variations in the elevations of the top of LBS points that reflect the presence (or absence) of large boulders or variations in consolidation of the sedimentary layers (Fig. 5D). The geotechnical drillings are also prone to the subjectiveness of the driller's interpretation of the top of LBS horizon which might result in slight variations in the elevation of the top of LBS points. Still, majority of the top of LBS points in the cross-sections follow a distinct laterally continuous horizon which we have interpreted as the top of the LBS (Fig. 10A–F).

5.2. Morphological signatures of the bedrock deformation zones and their network along the conventional bedrock-DEM

The deep central parts of the deformation zone intersections, the associated fracture-controlled vertical breaks within the conventional bedrock-DEM, and the correlation of the depressions with the deformation zone interpretations based on the other, 2D-datasets are clearly indicative that the bedrock surface depressions are associated with deformation zones within the underlying bedrock (Figs. 7, 8, 9, 10 A–E; Sections 4.2, 4.3, 4.4). For a limited number of the studied cross-sections, we were able to recognize and further delineate the occurrence of specific core domains and surrounding damage zones within the depressions (Figs. 10 A, B, D). In case the core domains are located at the center of the deformation zones (Figs. 10 A, D), the surrounding damage zones show symmetrical profile along the bedrock-DEM. In contrast, the damage zones show asymmetrical profile if the core domain is located on a side of the deformation zone (Fig. 10B). The width of the core domains is approximately 10–20 m in all the three cross-sections. For the remaining parts of the investigated deformation zones, the bedrock-DEM depressions were clearly recognized, and depth estimates generated, but no characterization of the internal structure could be conducted due to too few verified geotechnical bedrock surface points.

Correlation of the integrated 2D traces with the bedrock surface depressions along the conventional bedrock-DEM enabled us to understand the topology and lateral continuity (length) of the bedrock deformation zones within unexposed areas, which is crucial in analysis of the thicknesses of the LBS and overburden. The overall topological relationships of the bedrock deformation zones are roughly dichotomous. The northern and eastern study areas are dominated by several kilometers long zones with a few shorter zones that generally abut the longer ones at steep angles, whereas the western study area is characterized by more uniform-length, foliation-parallel, and foliation-perpendicular deformation zones that show both crossing and abutting topological relationships (Fig. 12).

The lateral continuities of the linear depressions along the conventional bedrock-DEM are discontinuous (Fig. 8) which we primarily attribute to the sparse character of the geotechnical bedrock surface points. We considered the correlation of the integrated 2D traces with the linear depressions as an improvement in constraining the lateral continuity of the deformation zones, with particular reference to the deepest parts of the linear depressions where very few verified geotechnical bedrock surface points are available. However, noteworthy is also the uncertainties of the source data used in compiling the integrated 2D traces. The geological and aeromagnetic maps (Figs. 7A–B) are inaccurate in the scale of tens of meters, which may be the width of the shorter deformation zones. The LiDAR traces (Fig. 7C) provide improved resolution, but they may be influenced by the intense anthropogenic activities within the urban area (e.g. sediment/rock mass fills, linear shapes of infrastructure). As such, the exact location of the deformation zones has a higher uncertainty than their existence and the character of the formed network.

The purpose of classifying the final deformation zone traces into the major, intermediate, and minor classes was to provide a practical tool to generate an improved version of the conventional bedrock-DEM. The classification and the following surface modification does not consider the interaction and intersection of the variably trending deformation zones and their damage zones, which typically are the sites of very intense fracturing (Peacock et al., 2017; Skyttä et al., 2023). As such, the distinct maxima within the overburden thickness observed at deformation zone intersections within the northern and eastern part of the study area (Fig. 12 A–B) are likely locations to even exceed the 19 m LBS thicknesses associated with the planar segments of deformations zones, providing a potential explanation to the up to 30 m thick till deposits reported in the earlier studies (Repo et al., 1970).

5.3. Usefulness of the structurally constrained bedrock-DEM and the associated sedimentary thicknesses

An overview of the thickness maps shows that the structurally constrained bedrock-DEM (Fig. 11B, D) significantly emphasizes the bedrock deformation zones as the areas of thickness maxima of the LBS and overburden compared to the thicknesses visualized using the conventional bedrock-DEM (Fig. 11A, C). At first, one might think that the deformation zones are overemphasized in the structurally constrained

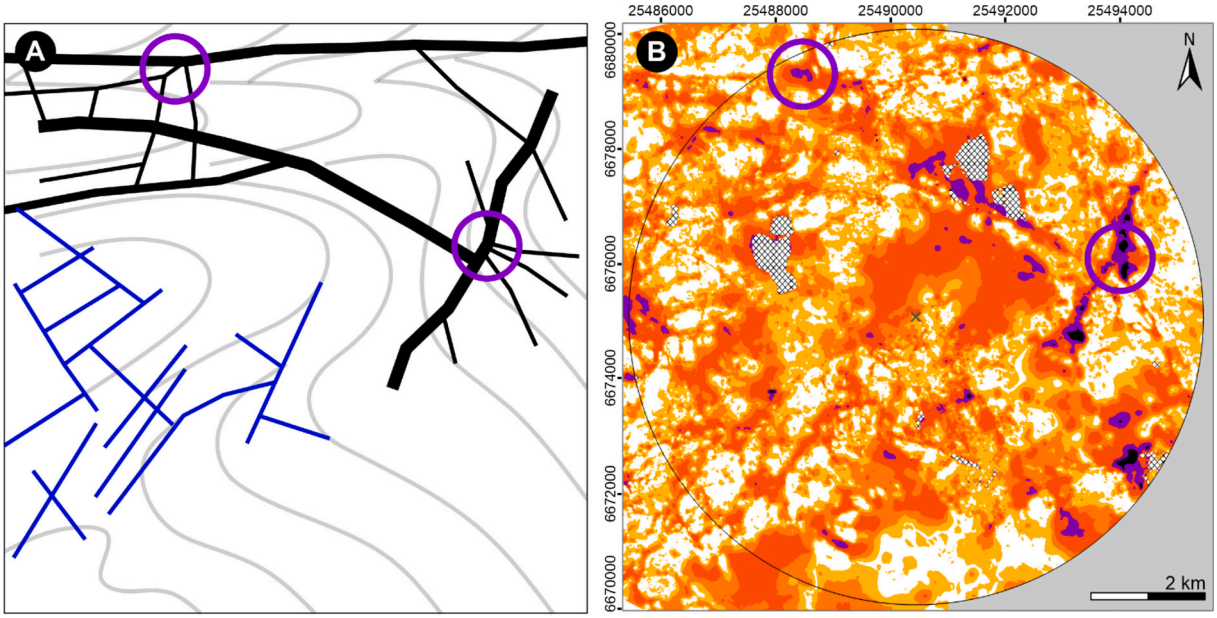

Fig. 12. A) Conclusive illustration of the major structural features within the study area based on simplification of the final deformation zone traces and ductile form lines. The major intersection areas of the bedrock deformation zones highlighted with purple circles. B) The areas of thickness maxima of the overburden correlate with deformation zone intersections. (For interpretation of the references to colour in this figure legend, the reader is referred to the web version of this article.)

bedrock-DEM but whether this is realistic or unrealistic situation, we need to consider how the erosion surface of the crystalline bedrock would look like if every overlying piece of boulder and sand grain were removed. The structurally constrained bedrock-DEM provides a sight into such situation.

The discontinuous character of the linear depressions along the conventional bedrock-DEM (Fig. 8) is most likely the result of the Ordinary Kriging interpolation generating zig-zag shapes or alternating high and low areas due to the few verified geotechnical bedrock surface points available within the bedrock deformation zones. As such, the conventional bedrock-DEM represents plain interpolation of the source data points without geological meaning. The structurally constrained bedrock-DEM reduces this uncertainty as the linear depressions were pulled down based on the observed LBS thicknesses (Section 3.2; Fig. 13), and the shape, length and termination points of the deformation zones were modified based on the correlation between the linear depressions and the constraints derived from the 2D structural analysis (Fig. 9). The pulling method also smoothened the bottoms of the linear depressions by removing any zig-zag shapes. Furthermore, we interpreted an elliptical shape for the bottoms of the linear depressions with the LBS thickness maxima at the center of the zones (VII in Fig. 6B) to reflect a typical along strike profile of a fault (Fig. 13). It is likely that the resulted linear depressions along the structurally constrained bedrock-DEM still have considerable uncertainties due to e.g., natural variations in the elevation of the bedrock erosion surface even within the deformation zones. However, the structurally constrained bedrock-DEM provides regionally continuous bedrock surface model which can be used in evaluation of the thicknesses of the sediments applied to various engineering applications.

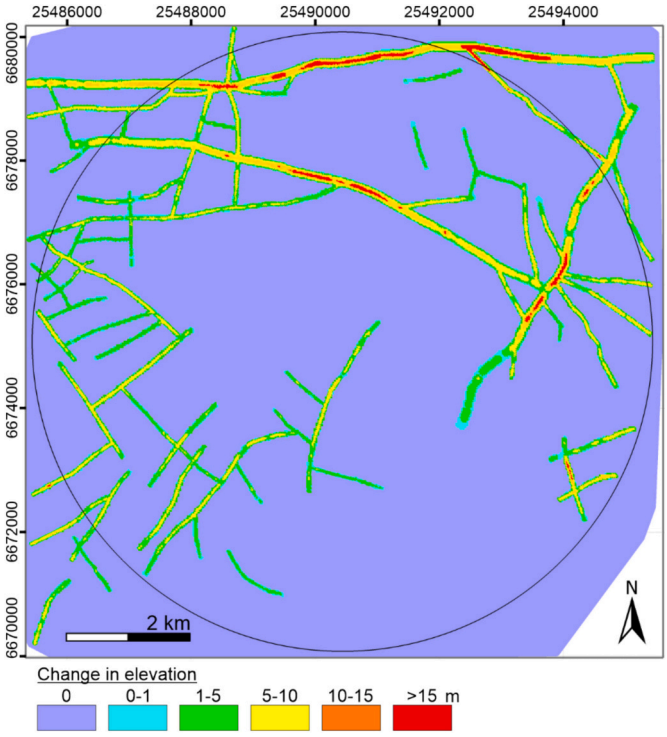

Fig. 13. Comparison of the elevation changes between the conventional and the structurally constrained bedrock-DEMs (a residual map). The largest changes show approximately at the center of the deformation zones highlighting a typical along strike profile of a fault. The areas outside the deformation zones remain unmodified.

6. Conclusions

- Geological models over the bedrock surface topography can be improved substantially by integrating the conventional bedrock surface elevation point data with i) the 2D-continuity and networking of bedrock deformation zones, ii) fracture-controlled erosional signatures of the deformation zones, and iii) the thickness of the overlying sediments (Sections 4.2, 4.3, 4.4).
- The improved, structurally constrained bedrock-DEM provides a regionally continuous and geologically justified model over the bedrock surface topography, and it reduces the epistemic uncertainty associated with the contribution of bedrock structures (Fig. 11).

- The glacial erosion and the subsequent *syn-* to post-glacial infill are localized into bedrock deformation zones which causes major local variations in the thickness of the LBS and overburden. We have shown that the LBS can be over 10 m thick above the damage zones and at least 19 m thick above the core domains of the major bedrock deformation zones, whereas the maximum LBS thickness outside the bedrock deformation zones was observed 3 m (Fig. 10).
- We presented a new method to analyze the architecture (damage zones, core domains) of bedrock deformation zones based the integration of geotechnical ground investigations and 2D-structural analysis (Fig. 10).
- Recommended future studies include sedimentological characterization of the overburden, and more detailed characterization of the deformation zones so that the intersection and interaction damage of the deformation zones segments are considered.

CRediT authorship contribution statement

Teemu Lindqvist: Writing – review & editing, Writing – original draft, Visualization, Validation, Software, Methodology, Investigation, Funding acquisition, Formal analysis, Data curation, Conceptualization. **Eemi Ruuska:** Writing – review & editing, Writing – original draft, Visualization, Validation, Software, Methodology, Investigation, Formal analysis, Data curation, Conceptualization. **Emilia Kosonen:** Writing – review & editing, Writing – original draft, Validation, Software, Resources, Project administration, Methodology, Investigation, Funding acquisition, Formal analysis, Data curation. **Noora Hornborg:** Validation, Software, Methodology, Data curation. **Pietari Skyttä:** Writing – review & editing, Writing – original draft, Visualization, Validation, Supervision, Software, Project administration, Methodology, Investigation, Formal analysis, Conceptualization. **Niko Putkinen:** Writing – review & editing, Writing – original draft, Validation, Supervision, Resources, Project administration, Methodology, Investigation, Funding acquisition, Conceptualization. **Juho Mansikkamäki:** Writing – review & editing, Validation, Supervision, Methodology, Conceptualization.

Declaration of competing interest

The authors declare that they have no known competing financial interests or personal relationships that could have appeared to influence the work reported in this paper.

Acknowledgements

Funding: This work was supported by Academy of Finland funded SEISMIC RISK project [Funding Decisions no. 339670] and GTK's project ‘Kestävä maankäyttö ja rakentaminen’.

We thank Jouni Lerssi, GTK for optimization of the aeromagnetic map for the 2D structural analysis, and Tuija Elminen and Nikolas Ovaskainen, both from GTK for comments that improved the text.

Appendix A. Supplementary cross-sections across and outside the bedrock deformation zones

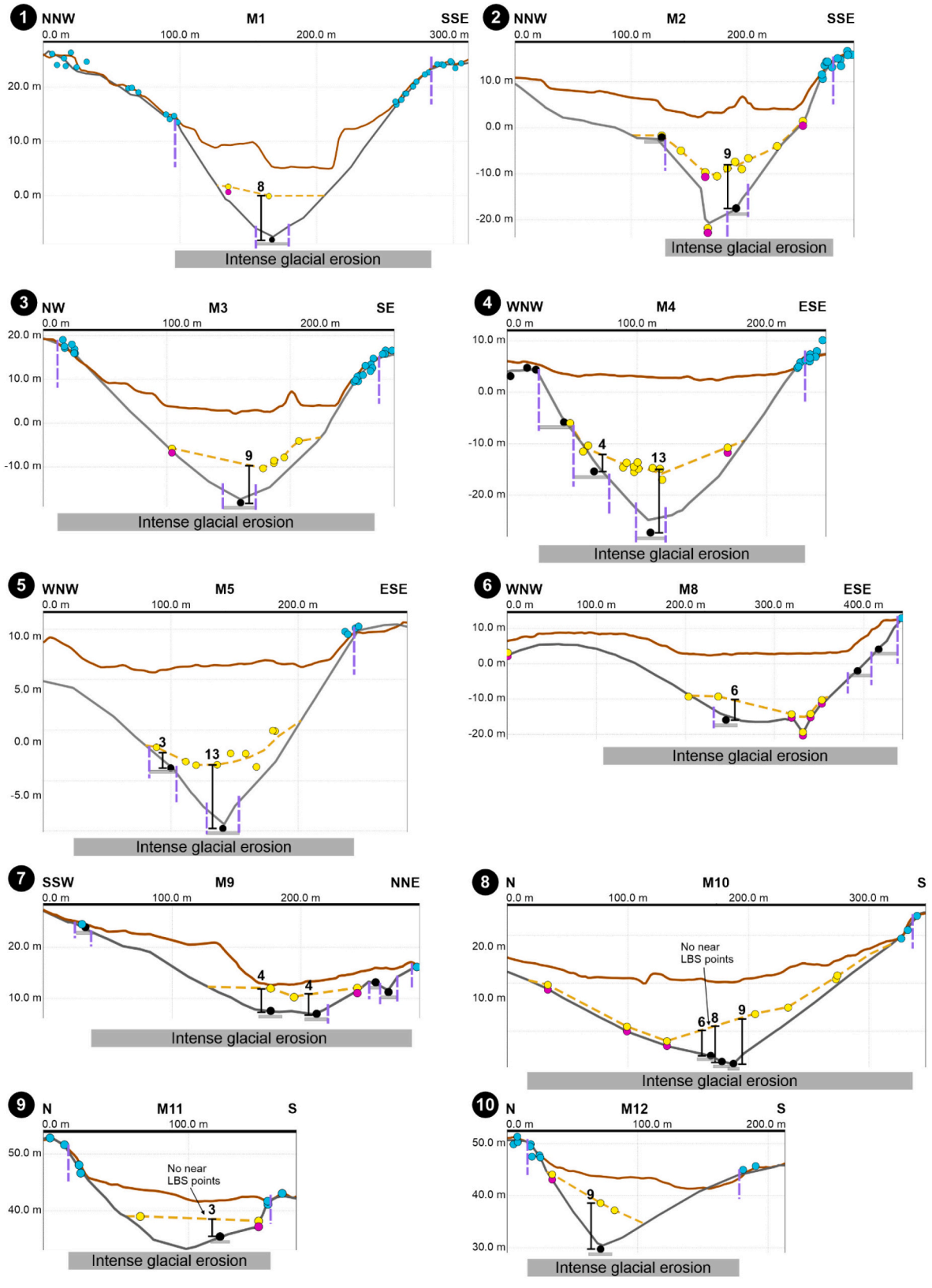
1
NNW
M1
SSE
0.0 m
100.0 m
200.0 m
300.0 m
20.0 m
10.0 m
0.0 m
8
Intense glacial erosion
2
NNW
M2
SSE
0.0 m
100.0 m
200.0 m
10.0 m
0.0 m
-10.0 m
-20.0 m
9
Intense glacial erosion
3
NW
M3
SE
0.0 m
100.0 m
200.0 m
20.0 m
10.0 m
0.0 m
-10.0 m
9
Intense glacial erosion
4
WNW
M4
ESE
0.0 m
100.0 m
200.0 m
10.0 m
0.0 m
-10.0 m
-20.0 m
4
13
Intense glacial erosion
5
WNW
M5
ESE
0.0 m
100.0 m
200.0 m
10.0 m
5.0 m
0.0 m
-5.0 m
3
13
Intense glacial erosion
6
WNW
M8
ESE
0.0 m
100.0 m
200.0 m
300.0 m
400.0 m
10.0 m
0.0 m
-10.0 m
-20.0 m
6
Intense glacial erosion
7
SSW
M9
NNE
0.0 m
100.0 m
200.0 m
20.0 m
10.0 m
4
4
Intense glacial erosion
8
N
M10
S
0.0 m
100.0 m
200.0 m
300.0 m
20.0 m
10.0 m
No near
LBS points
6
8
9
Intense glacial erosion
9
N
M11
S
0.0 m
100.0 m
50.0 m
40.0 m
No near
LBS points
3
Intense glacial erosion
10
N
M12
S
0.0 m
100.0 m
200.0 m
50.0 m
40.0 m
30.0 m
9
Intense glacial erosion

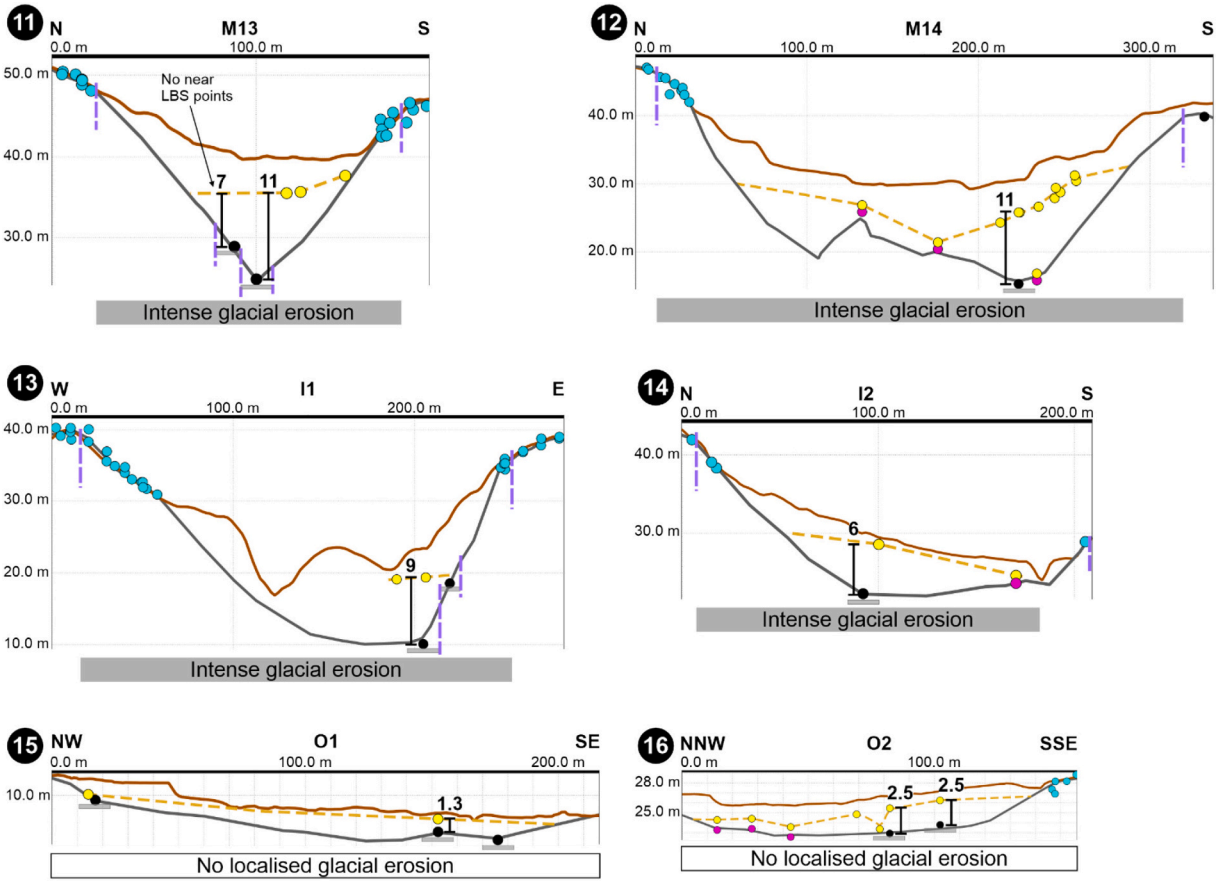

Data availability

The references of the used source datasets include information of the data availability. The resulted models are available upon reasonable request.

References

Abbaszadeh Shahri, A., Larsson, S., Renkel, C., 2020. Artificial intelligence models to generate visualized bedrock level: a case study in Sweden. Model. Earth Syst. Environ. 6, 1509–1528. https://doi.org/10.1007/s40808-020-00767-0.

Abbaszadeh Shahri, A., Shan, C., Zäll, E., Larsson, S., 2021. Spatial distribution modeling of subsurface bedrock using a developed automated intelligence deep learning procedure: a case study in Sweden. J. Rock Mech. Geotech. Eng. 13, 1300–1310. https://doi.org/10.1016/j.jrmge.2021.07.006.

Acoustic-seismic sub-bottom profiling data. Geological Survey of Finland. Data not openly available.

[dataset] Aeromagnetic anomaly map of Finland, 1972–2007. Version 1.0. Geological Survey of Finland, HAKKU service. Available at: https://hakku.gtk.fi/en/locations/search?location_id=6. Reference date 12th Feb. 2024.

Alley, R.B., Holschuh, N., MacAyeal, D.R., Parizek, B.R., Zoet, L., Riverman, K., Muto, A., Christianson, K., Clyne, E., Anandakrishnan, S., Stevens, N., GHOST Collaboration, 2021. Bedforms of Thwaites Glacier, West Antarctica: character and origin. Case Rep. Med. 126, e2021JF006339. https://doi.org/10.1029/2021JF006339.

Andrén, E., Andrén, T., Kunzendorf, H., 2000. Holocene history of the Baltic Sea as a background for assessing records of human impact in the sediments of the Gotland Basin. The Holocene 10, 687–702. https://doi.org/10.1191/09596830094944.

Baise, L.G., Kaklamanos, J., Berry, B.M., Thompson, E.M., 2016. Soil amplification with a strong impedance contrast: Boston, Massachusetts. Eng. Geol. 202, 1–13. https://doi.org/10.1016/j.enggeo.2015.12.016.

Baynes, F.J., Parry, S., Novotný, J., 2021. Engineering geological models, projects and geotechnical risk. Q. J. Eng. Geol. Hydrogeol. 54, qjegh2020-080. https://doi.org/10.1144/qjegh2020-080.

[dataset] Bedrock of Finland 1:10 000 000, 2019. Version 1.0. Geological Survey of Finland, HAKKU service. Available at: https://hakku.gtk.fi/en/locations/search?location_id=201. Reference date 12th Feb. 2024.

[dataset] Bedrock of Finland 1:200 000, 2022. Version 2.3. Geological Survey of Finland, HAKKU service. Available at: https://hakku.gtk.fi/en/locations/search?location_id=2. Reference date 12th Feb. 2024.

[dataset] Bedrock of Finland scale free, 2022. Version 2.3. Geological Survey of Finland, HAKKU service. Available at: https://hakku.gtk.fi/en/locations/search?location_id=181. Reference date 12th Feb. 2024.

[dataset] Bedrock weakness zones 1:50 000, 2020. Version 2.0. Geological Survey of Finland, HAKKU service. Available at: https://hakku.gtk.fi/en/locations/search?location_id=188. Reference date 12th Feb. 2024.

Benn, D., Evans, D.J.A., 2010. Glaciers and Glaciation, 2nd edition. Routledge, London, p. 816. https://doi.org/10.4324/9780203785010.

Björck, S., 1995. A review of the history of the Baltic Sea, 13.0-8.0 ka BP. Quat. Int. 27, 19–40. https://doi.org/10.1016/1040-6182(94)00057-C.

Bond, C.E., Johnson, G., Ellis, J.F., 2015. Structural model creation: the impact of data type and creative space on geological reasoning and interpretation. Geol. Soc. Lond. Spec. Publ. 421, 83–97. https://doi.org/10.1144/SP421.4.

Bouchard, M.A., Gibbard, P., Salonen, V.-P., 1990. Lithostratotypes for Weichselian and pre-Weichselian sediments in southern and western Finland. Bull. Geol. Soc. Finl. 62, 79–95. https://doi.org/10.17741/bgsf/62.1.005.

Bowden, R.A., 2004. Building confidence in geological models. Geol. Soc. Lond. Spec. Publ. 239, 157–173. https://doi.org/10.1144/GSL.SP.2004.239.01.11.

Cassidy, R., Comte, J.-C., Nitsche, J., Wilson, C., Flynn, R., Ofterdinger, U., 2014. Combining multi-scale geophysical techniques for robust hydro-structural characterisation in catchments underlain by hard rock in post-glacial regions. J. Hydrol. 517, 715–731. https://doi.org/10.1016/j.jhydrol.2014.06.004.

CEN, 2007. Eurocode 7 - Geotechnical Design - Part 2: Ground Investigation and Testing. European Committee for Standardisation, Brussels, p. 180.

Chesnaux, R., Lambert, M., Walter, J., Fillastre, U., Hay, M., Rouleau, A., Daigneault, R., Moisan, A., Germaneau, D., 2011. Building a geodatabase for mapping hydrogeological features and 3D modeling of groundwater systems: Application to the Saguenay–Lac-St.-Jean region, Canada. Comput. Geosci. 37, 1870–1882. https://doi.org/10.1016/j.cageo.2011.04.013.

Chesnaux, R., Lambert, M., Walter, J., Dugrain, V., Rouleau, A., Daigneault, R., 2017. A simplified geographical information systems (GIS)-based methodology for

modeling the topography of bedrock: illustration using the Canadian Shield. Appl. Geomat. 9, 61–78. https://doi.org/10.1007/s12518-017-0183-1.
Chetty, P., Tesfamichael, S., 2021. A comparison of interpolation techniques in producing a DEM from the 5 m National Geospatial Institute (NGI) contours. In: Proceedings of the 7th International Conference on Geographical Information Systems Theory, Applications and Management (GISTAM 2021), pp. 37–47. https://doi.org/10.5220/0010525100370047.
Chung, J., Rogers, J.D., 2012. Estimating the position and variability of buried bedrock surfaces in the St. Louis metro area. Eng. Geol. 126, 37–45. https://doi.org/10.1016/j.enggeo.2011.12.007.
Davis, J.C., 2002. Statistics and Data Analysis in Geology, 3rd ed. Wiley, New York, p. 656.
Donner, J., 1995. The Quaternary History of Scandinavia. Cambridge University Press, New York, p. 212.
Ehlers, C., Lindroos, A., Selonen, O., 1993. The late Svecofennian granite-migmatite zone of southern Finland—a belt of transpressive deformation and granite emplacement. Precambrian Res. 64, 295–309. https://doi.org/10.1016/0301-9268(93)90083-E.
Elevation model 2 m. National Land Survey of Finland. Available at: https://asiointi.maanmittauslaitos.fi/karttapaikka/tiedostopalvelu/korkeusmalli. Reference date 12th Feb. 2024.
Elminen, T., Airo, M.-L., Niemelä, R., Pajunen, M., Vaarma, M., Wasenius, P., Wennerström, M., 2008. Fault structures in the Helsinki area, southern Finland. In: Pajunen, M. (Ed.), Tectonic Evolution of the Svecofennian Crust in Southern Finland - a Basis for Characterizing Bedrock Technical Properties, Geological Survey of Finland, Special Paper 47, pp. 185–213.
Erdogan, S., 2009. A comparision of interpolation methods for producing digital elevation models at the field scale. Earth Surf. Process. Landf. 34, 366–376. https://doi.org/10.1002/esp.1731.
[dataset] Espoo, 1986. Map of Quaternary deposits. Web service: https://kartat.espoo.fi/IMS/en/Map. Data not openly available. Data received for the SEISMIC RISK project 1st Dec. 2020.
Evans, D.J.A., Phillips, E.R., Hiemstra, J.F., Auton, C.A., 2006. Subglacial till: Formation, sedimentary characteristics and classification. Earth Sci. Rev. 78, 115–176. https://doi.org/10.1016/j.earscirev.2006.04.001.
Eyles, N., Putkinen, N., Sookhan, S., Arbelaez-Moreno, L., 2016. Erosional origin of drumlins and megaridges. Sediment. Geol. 338, 2–23. https://doi.org/10.1016/j.sedgeo.2016.01.006.
Foliation observations. Compiled from databases of Geological Survey of Finland, City of Helsinki, City of Espoo. Data not openly available.
Geotechnical ground investigations-a. Compiled from databases of Cities of Helsinki and Espoo. Data not openly available. Data received for the SEISMIC RISK project 16th and 19th Feb. 2021.
Geotechnical ground investigations-b. Geological Survey of Finland. Available at: https://gtkdata.gtk.fi/Pohjatutkimukset/index.html. Reference date: 6th Sept. 2024.
Giacomelli, S., Zuccarini, A., Amorosi, A., Bruno, L., Di Paola, G., Martini, A., Severi, P., Berti, M., 2023. 3D geological modelling of the Bologna urban area (Italy). Eng. Geol. 324, 107242. https://doi.org/10.1016/j.enggeo.2023.107242.
Gong, J., Li, Z., Zhu, Q., HG, S., Zhou, Y., 2000. Effects of various factors on the accuracy of DEMs: an intensive experimental investigation. Photogramm. Eng. Remote. Sens. 66, 1113–1117.
Haavisto, M., Kukkonen, E., 1975. Geological map of Finland 1:100 000. Quaternary deposits in the Helsinki map-sheet area including sea bottom, Sheet 2034 Helsinki. Geological Survey of Finland, Espoo, p. 20 (in Finnish).
Haavisto-Hyvärinen, M., Stén, C.-G., Backman, B., 1996. Tapiolan maaperäkartan 2034 03 selitys. Geological Survey of Finland, Espoo, p. 12 (in Finnish).
Hall, A.M., Putkinen, N., Hietala, S., Lindsberg, E., Holma, M., 2021. Ultra-slow cratonic denudation in Finland since 1.5 Ga indicated by tiered unconformities and impact structures. Precambrian Res. 352, 106000. https://doi.org/10.1016/j.precamres.2020.106000.
Hanna, A., Mashhour, I., Nguyen, N., 2022. Drag load on End-Bearing Piles in Partially Saturated Collapsible Soil. Geotech. Geol. Eng. 40, 3431–3442. https://doi.org/10.1007/s10706-022-02098-6.
Heeremans, M., Wijbrans, J., 1999. Late Proterozoic tectonic events in southern Finland, constrained by 40 Ar/ 39 Ar incremental heating and single spot fusion experiments on K-feldspars. Terra Nova 11, 216–222. https://doi.org/10.1046/j.1365-3121.1999.00250.x.
[dataset] Helsinki, 2017. Soil Map. https://kartta.hel.fi/?setlanguage=en#. Data not openly available. Received from City of Helsinki for the SEISMIC RISK project 1th Dec.2020.
[dataset] Helsinki, 2019. Base Map. https://kartta.hel.fi/?setlanguage=en#. Data not openly available. Received from City of Helsinki for the SEISMIC RISK project 6th Apr. 2021.
Hirvas, H., Nenonen, K., 1987. The till stratigraphy of Finland. Geol. Surv. Finland Spec. Pap. 3, 49–63.
Hirvas, H., Lintinen, P., Lunkka, J.P., Eriksson, B., Grönlund, T., 1995. Sedimentation and lithostratigraphy of the Vuosaari multiple till sequence in Helsinki, southern Finland. Bull. Geol. Soc. Finl. 67, 51–64. https://doi.org/10.17741/bgsf/67.2.004.
Høyer, A.-S., Klint, K.E.S., Fiandaca, G., Maurya, P.K., Christiansen, A.V., Balbarini, N., Bjerg, P.L., Hansen, T.B., Møller, I., 2019. Development of a high-resolution 3D geological model for landfill leachate risk assessment. Eng. Geol. 249, 45–59. https://doi.org/10.1016/j.enggeo.2018.12.015.
Kähkönen, Y., 2005. Svecofennian supracrustal rocks. In: Lehtinen, M., Nurmi, P.A., Rämö, O.T. (Eds.), Precambrian Geology of Finland – Key to the Evolution of the Fennoscandian Shield. Elsevier B.V, Amsterdam, pp. 343–406.
Kim, K.-H., Seo, W., Han, J., Kwon, J., Kang, S.Y., Ree, J.-H., Kim, S., Liu, K., 2020. The 2017 ML 5.4 Pohang earthquake sequence, Korea, recorded by a dense seismic network. Tectonophysics 774, 228306. https://doi.org/10.1016/j.tecto.2019.228306.
Korsman, K., Koistinen, T., Kohonen, J., Wennerström, M., Ekdahl, E., Honkamo, M., Idman, H., Pekkala, Y. (Eds.), 1997. Bedrock Map of Finland 1:1 000 000. Geological Survey of Finland, Special Maps, p. 37.
Kosunen, P., 2004. Petrogenesis of Mid-Proterozoic A-Type Granites: Case Studies from Fennoscandia (Finland) and Laurentia (New Mexico). PhD thesis,. University of Helsinki, Department of Geology.
Krabbendam, M., Bradwell, T., 2014. Quaternary evolution of glaciated gneiss terrains: pre-glacial weathering vs. glacial erosion. Quat. Sci. Rev. 95, 20–42. https://doi.org/10.1016/j.quascirev.2014.03.013.
Lahtinen, R., Korja, A., Nironen, M., 2005. Paleoproterozoic tectonic evolution. In: Lehtinen, M., Nurmi, P.A., Rämö, O.T. (Eds.), Precambrian Geology of Finland – Key to the Evolution of the Fennoscandian Shield. Elsevier B.V, Amsterdam, pp. 481–532.
[dataset] Laser scanning data 0,5 p, 2008-2019. National Land Survey of Finland. Available at: https://asiointi.maanmittauslaitos.fi/karttapaikka/tiedostopalvelu/laserkeilausaineisto_05. Reference date 12th Feb. 2024.
Lee, E.M., 2016. Landslide risk assessment: the challenge of communicating uncertainty to decision-makers. Q. J. Eng. Geol. Hydrogeol. 49, 21–35. https://doi.org/10.1144/qjegh2015-066.
Lee, J.H., Van Nguyen, H., Choi, I.-K., Kim, J.H., 2021. Effects of Soil Amplification on Ground Motion Response Spectra with High-Frequency Contents at Generic Soil Sites for Nuclear Facilities in Korea. KSCE J. Civ. Eng. 25, 2394–2410. https://doi.org/10.1007/s12205-021-0767-5.
Lysdahl, A.K., Christensen, C.W., Pfaffhuber, A.A., Vöge, M., Andresen, L., Skurdal, G.H., Panzner, M., 2022. Integrated bedrock model combining airborne geophysics and sparse drillings based on an artificial neural network. Eng. Geol. 297, 106484. https://doi.org/10.1016/j.enggeo.2021.106484.
Madsen, R.B., Høyer, A.-S., Andersen, L.T., Møller, I., Hansen, T.M., 2022. Geology-driven modeling: a new probabilistic approach for incorporating uncertain geological interpretations in 3D geological modeling. Eng. Geol. 309, 106833. https://doi.org/10.1016/j.enggeo.2022.106833.
Mattila, J., Viola, G., 2014. New constraints on 1.7 Gyr of brittle tectonic evolution in southwestern Finland derived from a structural study at the site of a potential nuclear waste repository (Olkiluoto Island). J. Struct. Geol. 67, 50–74. https://doi.org/10.1016/j.jsg.2014.07.003.
Nordbäck, N., Mattila, J., Zwingmann, H., Viola, G., 2022. Precambrian fault reactivation revealed by structural and K-Ar geochronological data from the spent nuclear fuel repository in Olkiluoto, southwestern Finland. Tectonophysics 824, 229208. https://doi.org/10.1016/j.tecto.2022.229208.
Ojala, A.E.K., Virtasalo, J.J., Lindsberg, E., Markovaara-Koivisto, M., 2021. Basin-Scale 3D Sedimentary Modelling: an Approach to Subdivide Baltic Sea Onshore Sediments for Land use and Construction. Geotech. Geol. Eng. 39, 4855–4876. https://doi.org/10.1007/s10706-021-01799-8.
Olayanju, G.M., Mogaji, K.A., Lim, H.S., Ojo, T.S., 2017. Foundation integrity assessment using integrated geophysical and geotechnical techniques: case study in crystalline basement complex, southwestern Nigeria. J. Geophys. Eng. 14, 675–690. https://doi.org/10.1088/1742-2140/aa64f7.
Pajunen, M., Airo, M.-L., Elminen, T., Mänttäri, I., Niemelä, R., Vaarma, M., Wasenius, P., Wennerström, M., 2008. Tectonic evolution of the Svecofennian crust in southern Finland. In: Pajunen, M. (Ed.), Tectonic Evolution of the Svecofennian Crust in Southern Finland - a Basis for Characterizing Bedrock Technical Properties, Geological Survey of Finland, Special Paper 47, pp. 15–160.
Paulen, R., McClenaghan, M.B., Harris, J., 2006. Bedrock topography and drift thickness models from the Timmins area, northeastern Ontario: an application of GIS to the Timmins overburden drillhole database. In: GIS Applications in the Earth Sciences. Geological Association of Canada, pp. 413–434.
Peacock, D.C.P., Dimmen, V., Rotevatn, A., Sanderson, D.J., 2017. A broader classification of damage zones. J. Struct. Geol. 102, 179–192. https://doi.org/10.1016/j.jsg.2017.08.004.
Popovs, K., Kalvāns, A., Jemeljanova, M., Saks, T., Dēliņa, A., Bikše, J., Babre, A., Retiķe, I., 2022. Bedrock surface topography of Latvia. J. Maps 18, 370–381. https://doi.org/10.1080/17445647.2022.2067011.
Rainio, H., Lahermo, P., 1976. Observations on dark grey basal till in Finland. Bull. Geol. Soc. Finl. 48, 137–152. https://doi.org/10.17741/bgsf/48.1-2.011.
Repo, R., Valovirta, V., Rainio, H., 1970. Geological map of Finland 1:100 000. Explanation to the map of Quaternary deposits, Sheet 2032 Espoo. Geological Survey of Finland, Otaniemi, p. 35 (in Finnish).
Ruuska, E., Skyttä, P., Putkinen, N., Valjus, T., 2023. Contribution of bedrock structures to the bedrock surface topography and groundwater flow systems within deep glaciofluvial aquifers in Kurikka, Western Finland. Earth Surf. Process. Landf. 48, 2039–2056. https://doi.org/10.1002/esp.5602.
Salekin, S., Burgess, J., Morgenroth, J., Mason, E., Meason, D., 2018. A comparative study of three non-geostatistical methods for optimising digital elevation model interpolation. ISPRS Int. J. Geo Inf. 7, 300. https://doi.org/10.3390/ijgi7080300.
Sanderson, D.J., Nixon, C.W., 2015. The use of topology in fracture network characterization. J. Struct. Geol. 72, 55–66. https://doi.org/10.1016/j.jsg.2015.01.005.
Saresma, M., Kosonen, E., Ojala, A.E.K., Kaskela, A., Korkiala-Tanttu, L., 2021. Characterization of sedimentary depositional environments for land use and urban planning in Espoo, Finland. Bull. Geol. Soc. Finl. 93, 31–51. https://doi.org/10.17741/bgsf/93.1.003.
Setiawan, B., Jaksa, M., Griffith, M., Love, D., 2018. Estimating bedrock depth in the case of regolith sites using ambient noise analysis. Eng. Geol. 243, 145–159. https://doi.org/10.1016/j.enggeo.2018.06.022.

Skyttä, P., Mänttäri, I., 2008. Structural setting of late Svecofennian granites and pegmatites in Uusimaa Belt, SW Finland: Age constraints and implications for crustal evolution. Precambrian Res. 164, 86–109. https://doi.org/10.1016/j.precamres.2008.04.001.

Skyttä, P., Torvela, T., 2018. Brittle reactivation of ductile precursor structures: the role of incomplete structural transposition at a nuclear waste disposal site, Olkiluoto, Finland. J. Struct. Geol. 116, 253–259. https://doi.org/10.1016/j.jsg.2018.06.009.

Skyttä, P., Kinnunen, J., Palmu, J.-P., Korkka-Niemi, K., 2015. Bedrock structures controlling the spatial occurrence and geometry of 1.8Ga younger glacifluvial deposits — example from first Salpausselkä, southern Finland. Glob. Planet. Chang. 135, 66–82. https://doi.org/10.1016/j.gloplacha.2015.10.007.

Skyttä, P., Nordbäck, N., Ojala, A., Putkinen, N., Aaltonen, I., Engström, J., Mattila, J., Ovaskainen, N., 2023. The interplay of bedrock fractures and glacial erosion in defining the present-day land surface topography in mesoscopically isotropic crystalline rocks. Earth Surf. Process. Landf. 48, 1956–1968. https://doi.org/10.1002/esp.5596.

Spadi, M., Tallini, M., Albano, M., Cosentino, D., Nocentini, M., Saroli, M., 2022. New insights on bedrock morphology and local seismic amplification of the Castelnuovo village (L'Aquila Basin, Central Italy). Eng. Geol. 297, 106506. https://doi.org/10.1016/j.enggeo.2021.106506.

Stephens, M.B., Follin, S., Petersson, J., Isaksson, H., Juhlin, C., Simeonov, A., 2015. Review of the deterministic modelling of deformation zones and fracture domains at the site proposed for a spent nuclear fuel repository, Sweden, and consequences of structural anisotropy. Tectonophysics 653, 68–94. https://doi.org/10.1016/j.tecto.2015.03.027.

Stroeven, A.P., Hättestrand, C., Kleman, J., Heyman, J., Fabel, D., Fredin, O., Goodfellow, B.W., Harbor, J.M., Jansen, J.D., Olsen, L., Caffee, M.W., Fink, D., Lundqvist, J., Rosqvist, G.C., Strömberg, B., Jansson, K.N., 2016. Deglaciation of Fennoscandia. Quat. Sci. Rev. 147, 91–121. https://doi.org/10.1016/j.quascirev.2015.09.016.

[dataset] Superficial deposits 1:100 000, 2015. Version 1.0. Geological Survey of Finland, HAKKU service. Available at: https://hakku.gtk.fi/en/locations/search?location_id=115. Reference date 12th Feb. 2024.

[dataset] Superficial deposits 1:20 000, 2015. Version 1.0. Geological Survey of Finland, HAKKU service. Available at: https://hakku.gtk.fi/en/locations/search?location_id=1. Reference date 12th Feb. 2024.

Sutinen, R., Hyvönen, E., Markovaara-Koivisto, M., Middleton, M., Ojala, A.E.K., Palmu, J.-P., Ruskeeniemi, T., Mattila, J., 2021. Glacially Induced Faults in Finland. In: Steffen, H., Olesen, O., Sutinen, R. (Eds.), Glacially-Triggered Faulting. Cambridge University Press, pp. 231–245. https://doi.org/10.1017/9781108779906.017.

Thierry, P., Prunier-Leparmentier, A.-M., Lembezat, C., Vanoudheusden, E., Vernoux, J.-F., 2009. 3D geological modelling at urban scale and mapping of ground movement susceptibility from gypsum dissolution: the Paris example (France). Eng. Geol. 105, 51–64. https://doi.org/10.1016/j.enggeo.2008.12.010.

Topographic database. National Land Survey of Finland. Available at: https://asiointi.maanmittauslaitos.fi/karttapaikka/tiedostopalvelu/maastotietokanta. Reference date 29th Feb. 2024.

Torvela, T., Kurhila, M., 2022. Timing of syn-orogenic, high-grade transtensional shear zone formation in the West Uusimaa Complex, Finland. Bull. Geol. Soc. Finl. 94, 5–22. https://doi.org/10.17741/bgsf/94.1.001.

Torvela, T., Mänttäri, I., Hermansson, T., 2008. Timing of deformation phases within the South Finland shear zone, SW Finland. Precambrian Res. 160, 277–298. https://doi.org/10.1016/j.precamres.2007.08.002.

Väisänen, M., Skyttä, P., 2007. Late Svecofennian shear zones in southwestern Finland. GFF 129, 55–64. https://doi.org/10.1080/11035890701291055.

Van Hoesen, J., 2014. A geographic information systems (GIS)-based approach to derivative map production and visualizing bedrock topography within the town of Rutland, Vermont, USA. ISPRS Int. J. Geo Inf. 3, 130–142. https://doi.org/10.3390/ijgi3010130.

Virtasalo, J.J., Schröder, J.F., Luoma, S., Majaniemi, J., Mursu, J., Scholten, J., 2019. Submarine groundwater discharge site in the first Salpausselkä ice-marginal formation, South Finland. Solid Earth 10, 405–423. https://doi.org/10.5194/se-10-405-2019.

Wennerström, M., Airo, M.-L., Elminen, T., Niemelä, R., Pajunen, M., Vaarma, M., Wasenius, P., 2008. Orientation and properties of jointing in Helsinki area, southern Finland. In: Pajunen, M. (Ed.), Tectonic Evolution of the Svecofennian Crust in Southern Finland - a Basis for Characterizing Bedrock Technical Properties, Geological Survey of Finland, Special Paper 47, pp. 253–282.

Yan, W., Shen, P., Zhou, W.-H., Ma, G., 2023. A rigorous random field-based framework for 3D stratigraphic uncertainty modelling. Eng. Geol. 323, 107235. https://doi.org/10.1016/j.enggeo.2023.107235.

Zimmerman, D., Pavlik, C., Ruggles, A., Armstrong, M.P., 1999. An experimental comparison of ordinary and universal kriging and inverse distance weighting. Math. Geol. 31, 375–390. https://doi.org/10.1023/A:1007586507433.